TU Delft

Delft University of Technology

Antimicrobial properties dependence on the composition and architecture of copper-alumina coatings prepared by plasma electrolytic oxidation (PEO)

Santos, Janaina S.; Márquez, Victor; Buijnsters, Josephus G.; Praserthdam, Supareak; Praserthdam, Piyasan

DOI
10.1016/j.apsusc.2022.155072

Publication date
2023

Document Version
Final published version

Published in
Applied Surface Science

Citation (APA)
Santos, J. S., Márquez, V., Buijnsters, J. G., Praserthdam, S., & Praserthdam, P. (2023). Antimicrobial properties dependence on the composition and architecture of copper-alumina coatings prepared by plasma electrolytic oxidation (PEO). *Applied Surface Science*, *607*, Article 155072. https://doi.org/10.1016/j.apsusc.2022.155072

Important note
To cite this publication, please use the final published version (if applicable).
Please check the document version above.

Copyright
Other than for strictly personal use, it is not permitted to download, forward or distribute the text or part of it, without the consent of the author(s) and/or copyright holder(s), unless the work is under an open content license such as Creative Commons.

Takedown policy
Please contact us and provide details if you believe this document breaches copyrights.
We will remove access to the work immediately and investigate your claim.

This work is downloaded from Delft University of Technology.
For technical reasons the number of authors shown on this cover page is limited to a maximum of 10.

Green Open Access added to TU Delft Institutional Repository

'You share, we take care!' - Taverne project

https://www.openaccess.nl/en/you-share-we-take-care

Otherwise as indicated in the copyright section: the publisher is the copyright holder of this work and the author uses the Dutch legislation to make this work public.

Applied Surface Science 607 (2023) 155072

Contents lists available at ScienceDirect

Applied Surface Science

journal homepage: www.elsevier.com/locate/apsusc

Full Length Article

Antimicrobial properties dependence on the composition and architecture of copper-alumina coatings prepared by plasma electrolytic oxidation (PEO)

Janaina S. Santos [a], Victor Márquez [a], Josephus G. Buijnsters [b], Supareak Praserthdam [c], Piyasan Praserthdam [a,*]

[a] Center of Excellence on Catalysis and Catalytic Reaction Engineering, Department of Chemical Engineering, Faculty of Engineering, Chulalongkorn University, Bangkok 10330, Thailand

[b] Department of Precision and Microsystems Engineering, Research Group of Micro and Nano Engineering, Delft University of Technology, Mekelweg 2, 2628 CD Delft, the Netherlands

[c] High-Performance Computing Unit (CECC-HCU), Center of Excellence on Catalysis and Catalytic Reaction Engineering (CECC), Chulalongkorn University, Bangkok 10330, Thailand

ARTICLE INFO

Keywords:
PEO coatings
Antimicrobial surfaces
Alumina
Copper
Porous films
Corrosion resistance

ABSTRACT

This study presents environmentally friendly and low-cost synthetic routes to produce antimicrobial coatings over 5052 Al alloy based on plasma electrolytic oxidation (PEO) technology. Two methodologies were explored: the decoration with copper and anodic doping with copper ions. The porous oxide layers produced in silicate media presented two porous layers consisting of γ-Al_2O_3 crystalline phase and amorphous phases of aluminosilicate, silica, and $Al(OH)_3$. Small amounts of copper (<0.3 at.%) were detected in the PEO films. In the Cu-decorated film, copper clusters composed of Cu^0 and Cu^{2+} species were observed visually as small black dots on the surface. In the Cu-doped film, the Cu^{2+} and Cu^+ species were homogeneously distributed on the surface. The copper content affected the corrosion performance in aggressive corrosive media. The PEO coatings showed a remarkable antimicrobial activity after 24 h in standard tests. The antimicrobial effectiveness of the Cu-decorated sample was higher against *S. aureus*, while the Cu-doped sample was more effective against *E. coli*. The results demonstrated that differences in the PEO coating architecture can affect the material composition and, consequently, the bacterial inactivation mechanism. These findings can serve as a guide to tailor aluminum alloys for specific antimicrobial surfaces.

1. Introduction

The Covid-19 pandemic demonstrated that the exposition to microorganisms could be critical and lead to a quick evolution of diseases and epidemic situations. Like viruses, resistant pathogenic bacteria can also present a high risk for human health. In this sense, material surfaces with antimicrobial properties could be helpful not only in healthcare facilities, hospitals, and medical utensils, but also in public spaces like transport, food courts, markets, malls, hotels, office buildings, and schools, especially in hand-washing tanks, reservoirs, vessels, pipes, doors, handrails and knobs, and household materials. Besides the contamination, some bacteria can induce bacteria adhesion over the surface, forming a biofilm and turning the material more susceptible to corrosion, particularly if the surface is in contact with an aqueous or wet environment [1]. In this sense, coatings produced over metals with antimicrobial properties and corrosion resistance can be attractive for several applications, including self-disinfecting surfaces.

The 5xxx aluminum alloy series are known for high magnesium content (2 %), high corrosion resistance, durability, good forming, and weldability [2]. They can be used to manufacture several utensils and offer an antimicrobial surface after a suitable surface treatment like the plasma electrolytic oxidation (PEO) technique. The PEO is a simple, scalable technique that uses a low number of chemicals to produce a protective, dense, and highly adherent ceramic coating on a wide range of metal surfaces. The high corrosion resistance, surface hardness, chemical stability, and high thermal stability of aluminum oxide PEO

* Corresponding author.
E-mail address: piyasan.p@chula.ac.th (P. Praserthdam).

https://doi.org/10.1016/j.apsusc.2022.155072
Received 12 June 2022; Received in revised form 20 September 2022; Accepted 23 September 2022
Available online 29 September 2022
0169-4332/© 2022 Elsevier B.V. All rights reserved.

coatings [3,4] make them attractive for several industrial applications, increasing the materials' lifetime. Regarding antimicrobial PEO surfaces, most of the studies in the literature are devoted to implant materials and photocatalysts for microbial inactivation, especially using Mg and Ti alloys as substrates [5,6]. The relative numbers of studies using Al alloys as a precursor for antimicrobial PEO coatings are low.

Different from conventional anodization, the PEO treatment is performed under voltages higher than the dielectric breakdown potential of the oxide. The coating properties can be controlled by the applied current/voltage (AC, DC, or pulsed modes), treatment time, electrolyte composition, and temperature [7–9]. The process is characterized by the appearance of visible electrical discharges blinking over the electrode, intense gas evolution, and Joule heating effect [10,11]. Due to the discharge characteristics, this technique is also known in the scientific literature as microarc oxidation (MAO) technique [12,13].

The breakdown events on the electrode surface like electrical discharges, gas evolution, and oxide dissolution are responsible for forming an irregular porous morphology due to the oxide melting/solidification process and particles ejection from the bulk to the oxide/electrolyte interface [7,8]. Depending on the discharge type, the electron plasma temperatures can vary from 3300 K to 10000 K [14]. The high temperature of the discharges can favor the *in-situ* crystallization of the oxide and the incorporation of the electrolyte species influencing the final oxide composition. In this sense, it is possible to assert that the electrical discharge properties can control morphology and microstructure.

Copper is one of the most used biocides exhibiting excellent antibacterial and antifouling properties [3,15] in a wide range of surface materials, and it can also be employed in PEO coatings. The common strategies to incorporate copper species into the oxide layer of the PEO coating are using Al-Cu alloys as the metal precursor substrate [16–20] or adding copper species into the electrolyte during the anodization [3,15,21]. On the other hand, when the purpose is to fabricate a heterojunctioned material, a copper plating procedure can be performed after the anodization [22], forming a metallic layer over the oxide coating. The choice of a suitable methodology to produce alumina PEO coating containing copper will depend on the application. The addition of copper chemicals in the PEO electrolyte can be used when the aluminum alloy substrate does not contain copper in its composition. It is commonly applied to improve specific properties of the anodic oxide layer like thermal radiation performance [21], corrosion resistance [3,21], and antifouling properties [3,15]. The copper plating methods after anodization are usually applied to form electrically conductive layers and improve the thermal conductivity and ductility of the PEO coating [22].

This study proposes a simple, environmentally friendly, low-cost synthetic route based on the PEO technique for fabricating films over aluminum for antimicrobial surface applications. We describe for the first time how the differences in the material architecture and composition can affect the bacterial inactivation mechanisms. Two methodologies were adopted to introduce small amounts of copper into alumina PEO coatings. An adapted copper plating method was employed to prepare Cu-decorated alumina PEO coating, and anodic doping [23] was used to insert Cu species into the oxide layer. The morphology, composition, microstructure, and wettability of the coatings were investigated and compared. The corrosion performance and antimicrobial activity were evaluated. The outcomes and important findings are discussed, considering the advances in the PEO technology field.

2. Experimental section

2.1. PEO coating synthesis

The oxide coatings were grown over aluminum specimens (96 %, 3 cm × 1 cm × 1 mm in size) by anodizing 5052 aluminum alloy substrates (Chokchai All Metal Service Co.) under PEO conditions. The experiments were conducted in silicate-based electrolyte maintained under agitation by a magnetic stirrer in a 100 mL jacketed glass cell coupled to a thermostatic bath to control the electrolyte temperature at 18 °C to prevent overheating of the electrochemical system during the PEO treatment. The bottom part of the Al substrate (1 cm × 1 cm × 1 mm) was immersed in 40 mL of electrolyte and placed between two stainless steel foils used as cathode. Before the experiments, the aluminum substrates were mechanically polished with #400, #600, and #1200 SiC emery papers and degreased in DI water and ethanol under sonication for 10 min each solvent.

The anodization was performed using a DC power supply (Wemaxpower WMX-ASD10001) under potentiodynamic and potentiostatic regimes. After reaching the potentiostatic condition, the anodization was maintained at the limiting voltage (350 V or 370 V) for 20 min. This restrained the PEO condition to spark-type discharges, promoting the oxide crystallization without destroying the films [11]. The voltage and current were monitored during the process by two multimeters (Agilent 34401A) connected in parallel and series to the electrochemical system. Details of the alloy substrate, the micrograph of the bare substrate after mechanical polishing, and the anodizing apparatus can be found in the supporting material (see appendices A and B – SI file).

All solutions were prepared with deionized water (Milli-Q®, >16 MΩ) and analytical-grade reagents (Sigma-Aldrich® and Univar®). The conditions used to produce the coatings are listed in Table 1. A 0.08 M Na_2SiO_3 + 0.05 M NaOH solution was used as electrolyte to prepare the copper-free anodized film films (from here onwards, referred to as sample A). Moderate values of Na_2SiO_3 and OH^- concentration were chosen to avoid a high rugosity coating due to the silicate content [24]. To prepare the Cu-decorated coating (sample B), samples produced in Na_2SiO_3 + NaOH solution were modified by copper electrodeposition after the anodization. In this case, the anodized film was used as the cathode for electrodeposition of copper in 0.05 M $Cu(NO_3)_2$ solution at room temperature. The electrodeposition step was carried out at −2 V for 10 min at room temperature using two copper foils as anodes.

A 0.08 M Na_2SiO_3 solution containing 0.002 M $Cu(NO_3)_2$ and 0.002 M ethylenediaminetetraacetic acid (EDTA) was used for doping the alumina films with copper (sample C). In this case, copper ions were complexed in an anionic complex to ease their migration towards the anode instead of the cathode. It is an alternative to avoid dispersing Cu_xO powders in the electrolyte [5], which increases the solution resistance and PEO voltage. NaOH was disregarded in this condition since its addition led to precipitation of $Cu(OH)_2$, forming a suspension that affected the reproducibility of the experiments. The pH value did not change significantly in the absence of NaOH, remaining around ~ 12. The EDTA was added into the solution to chelate Cu^{2+} ions forming $Cu(EDTA)^{2-}$ species [25], favoring their migration toward the anode.

Table 1
Experimental conditions of the fabrication of the alumina PEO coatings over AA5052 substrates.

Sample – Coating		Synthesis	Modification
A	Alumina film	Anodizing in 0.08 M Na_2SiO_3 + 0.05 M NaOH solution (pH 12.6) at 18 °C. Limiting voltage: 350 V, 20 min under potentiostatic control.	No
B	Cu-decorated alumina film	Anodizing in 0.08 M Na_2SiO_3 + 0.05 M NaOH solution (pH 12.6) at 18 °C. Limiting voltage: 350 V, 20 min under potentiostatic control.	Electrodeposition in 0.05 M $Cu(NO_3)_2$ (pH 4.6) at −2 V for 10 min
C	Cu-doped alumina film	Al anodizing in 0.08 M Na_2SiO_3 + 2 mM $Cu(NO_3)_2$ + 2 mM EDTA solution (pH 12.4) at 18 °C. Limiting voltage: 370 V, 20 min under potentiostatic control.	No

2.2. Material characterization

The morphology and composition of the anodic films were evaluated by using scanning electron microscopy (SEM) and energy-dispersive X-ray spectroscopy (EDX) using an AMICUS photoelectron spectrometer with an Mg Kα X-ray source controlled by KRATOS VISION2 software at 20 mA and 10 keV. The samples are mounted horizontally in the holder using carbon tape for the SEM top-view images. For the side-view images, the samples were cut exposing the cross-sectional view of the coating. These samples were mounted vertically in the holder using carbon tape. The grazing incident X-ray diffraction (GIXRD) analyses were performed at an incident angle of $\theta = 0.4^{\circ}$ using a Rigaku TTRAX III diffractometer with a Cu K α1 (1.544 Å) irradiation. MDI Jade 9 software was used to analyze the data, and ICDD PDF-2 (2021) was used as database. For X-ray photoelectron spectroscopy (XPS) analysis, the samples were cut in 0.5 cm × 0.8 cm × 0.1 cm dimensions and mounted with carbon tape in the holder of an Axis Supra spectrometer (Kratos®) using Mg Kα X-ray radiation (1253.6 eV) at a voltage of 10 kV and current of 20 mA. The spectra were acquired with pass energy of 75 eV. The binding energy value was calibrated by the C 1 s peak at 285 eV, and the elements Al 2p (74.8 eV), Si 2p (102.8 eV), O 1 s (532 eV), Cu 2p1 (933.3 eV), and Cu 2p2 (952.9 eV). The chemical bond properties of the films were analyzed by Fourier transform infrared spectroscopy (FTIR; Thermo Nicolet 6700). The Raman spectroscopy analysis was carried out using a Raman microscope Horiba XploRA Plus under the following conditions: 10 s acquisition time, 10 accumulations, x100 LWD objective, 532 nm laser excitation, 600 grating, 500 μm hole, 200 μm slit, and 0.1 % filter.

The wettability of the surfaces was evaluated by CA measurements using an adapted Tantec CAM-Image Optical Contact Angle meter, where the image analysis was performed by ImageJ® software using the contact angle plugin [26]. Water droplets of 0.5 μL volume were dropped at different points on the samples. The images were registered in a static mode, where three droplets per sample and three images per droplet were considered for the average deviation calculation. The images were taken at 5–10 s after the droplet reached the sample surface.

2.3. Corrosion performance evaluation

The corrosion performance was evaluated in polarized and steady-state conditions by potentiodynamic polarization (PDP) tests and electrochemical impedance spectroscopy (EIS). The electrochemical experiments were performed in a 3-electrode configuration cell coupled to a Multi Autolab/M204 potentiostat (Metrohm®) using a 3 wt% NaCl (pH 6.2) solution at room temperature as electrolyte. The anodized aluminum plates were used as working electrodes, a platinized Ti mesh was used as a counter-electrode, and an Ag/AgCl electrode in 3.0 M KCl was used as reference electrode (Metrohm®). The polarization measurements were carried out from −1.1 V to 1.3 V *vs* Ag/AgCl at a scan rate of 1 mV s^{-1} after 120 min of immersion under open circuit potential (OCP). The potential values in the plots were converted to the SHE potential scale considering the pH of the saline solution. The corrosion potential and corrosion current density were extracted from polarization curves by the Tafel extrapolation method. The inductively coupled plasma-optical emission spectrometry (ICP-OES) technique was employed to measure the leaching of metals in the solution after the PDP tests using an Optima 2100 DV Spectrometer from Perkin Elmer. For this, a total of 20 mL solution was collected after the PDP tests for the chemical analysis, performed in triplicate. For EIS measurements, a sinusoidal AC perturbation of 10 mV was applied to the electrodes in the frequency range from 0.1 to 1×10^5 Hz at OCP after 24 h of immersion in the chloride solution. The current and impedance values were normalized by the geometric area of the electrodes (2.3 cm^2) exposed to the electrolyte.

2.4. Antimicrobial tests

The antimicrobial tests were performed at the Laboratory Service from the Department of Microbiology, Faculty of Science, Chulalongkorn University (Thailand), following a modified Japan industrial standard test JIS Z 2801:2006 [1,27]. *Escherichia coli* (gram-negative) and *Staphylococcus aureus* (gram-positive) bacteria were grown in a standardized culture medium. The initial concentration of the microorganism suspension was adapted for the anodized aluminum specimen's size. Thus, 0.1 mL of the test inoculum was placed into each specimen in Petri dishes, covered with a sterilized film, and spread onto the sample surface. The Petri dishes containing the tested samples (triplicates) were inoculated with the test inoculum at 37 °C and 90 % humidity for 24 h. After the incubation period, the bacteria colonies were washed out, diluted, and plated for the determination of the microbial concentrations. The number of viable cells was estimated indirectly using the plate counting method [28] and expressed in CFU/mL. The percent reduction of bacteria was determined by Eq. (1):

$$\%\ reduction = \frac{(C_{24h} - C_{0h}) \times 100}{C_{0h}} \quad (1)$$

where C is the bacteria concentration in CFU/mL before treatment (0 h) or after treatment (24 h). The antimicrobial activity was evaluated by comparison between the results and a controlled experiment (untreated test pieces) obtained after 24 h using Eq. (2) [29]:

$$Antimicrobial\ activity = \log(C_{u,24h}) - \log(C_{PEO,24h}) \quad (2)$$

where $C_{u,24h}$ is the logarithm of the average bacteria concentration inoculated on untreated test pieces after 24 h (controlled experiment), and $C_{PEO,24h}$ is the logarithm of the average bacteria concentration after inoculation on PEO tests samples after 24 h; values equal to or higher than 2 indicate antimicrobial effectiveness.

3. Results and discussion

3.1. Synthesis and characterization of PEO oxide coatings on Al substrate

The Al specimens were anodized in alkaline silicate media under PEO conditions, and the voltage and current were monitored during the process. Fig. 1 depicts the voltage–time and current–time curves of the Al anodization in the conditions described in Table 1. The anodization was conducted in two regimes. In the former case, both current and voltage varied in response to the anodic oxidation of the aluminum. In the second regime, the oxide growth proceeded at a constant limiting voltage for 20 min: 350 V (samples A and B) and 370 V (sample C). These conditions maintained the system under the spark regime: the voltage was high enough to produce a sustainable sparking condition during the PEO treatment time without extinguishing itself but not so high as to consume too much power and lead to a microarcing regime [11,30].

Three regions characterized these profiles: (*i*) the rapid voltage increase from $t = 0$ to the breakdown potential (E_b); (*ii*) above the E_b, where the oxide growth rate decreased and the breakdown events occurred [10,11]; (*iii*) potentiostatic regime. The three samples exhibited the same profile, but sample C, produced in $Na_2SiO_3 + Cu(NO_3)_2 +$ EDTA solution, reached the potentiostatic condition faster (~25 min) than the experiments performed in $Na_2SiO_3 +$ NaOH (~47 min). The alkali content in the electrolyte is usually employed to increase oxygen content and enhance conductivity. But the OH^- ions also favor the oxide dissolution reaction decreasing the overall growth rate of the coating [31]. Since the formation of the PEO coating resulted from the competing oxide growth and oxide dissolution reactions, the absence of the NaOH led to the faster oxide growth of sample C.

Region (*i*) is characterized by a rapid voltage increase promoted by the enlargement of the compact oxide layer (barrier film). Due to the dielectric nature of the oxide film, the voltage increased as a response to

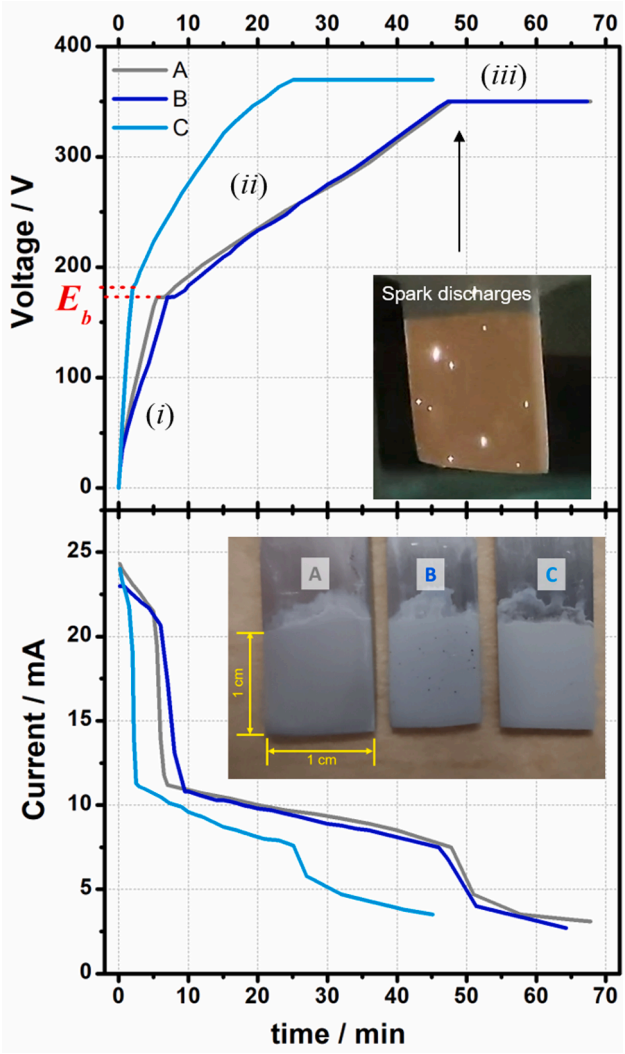

Fig. 1. Voltage and current as function of time monitored during the Al anodization under PEO conditions in 0.08 M Na_2SiO_3 + 0.05 M NaOH at 18 °C (samples A and B) and in 0.08 M Na_2SiO_3 + 2 mM $Cu(NO_3)_2$ + 2 mM EDTA at 18 °C (sample C). Top-inset: a night-vision image of the spark discharges on the electrode surface during PEO. Bottom-inset: images of the three samples after synthesis. E_B denotes the breakdown potential, and (*i*), (*ii*), (*iii*) refer to the different anodizing stages.

the increasing resistance. The primary reaction occurring was the anodic oxidation of the metallic Al substrate to Al_2O_3 at anodizing rates of 380 mV s^{-1} and 1540 mV s^{-1} in the Cu-free and Cu-content electrolytes, respectively (see Fig. B.2 in SI file). In the early stages, the current was majority ionic and decreased with time. As the reaction proceeded, a deviation from faradaic behavior [32] was observed in voltage *vs* time curves indicating that the electronic current, one of the precursors of the oxide breakdown events [33,34], became significant.

The oxide's breakdown potential (E_b) was observed at 172.8 V and 182.8 V in the experiments performed in Na_2SiO_3 + NaOH electrolyte and Na_2SiO_3 + $Cu(NO_3)_2$ + EDTA electrolyte, respectively. The E_b remained constant for approximately 1 min in the Cu-free solution while the current dropped from 20 mA to 11 mA. In the Cu-containing electrolyte, the potential remained at 182.8 V for ~ 25 s. The sharper current decay at E_b resulted from the oxide resistance reduction due to the formation of the channels/pores through the film.

The anodization rate decreased after reaching the E_b, as observed by the slope change in the region (*ii*) of the plots (Fig. B.2). The first visible sparks were observed at approximately 330 V in alkaline silicate solution and ~ 360 V in Cu-content electrolyte. The appearance of the first sparks in the region (*ii*) is accompanied by another change in the anodizing rates, indicating the intensification of the breakdown events [11]. After reaching the limiting voltage, the system was maintained under spark regime until the end of the experiment (region *iii*). The top-inset of Fig. 1 shows the spark discharges on the Al surface during the anodization of sample A in region (*iii*), and the bottom-inset depicts the images of the three synthesized coatings over the aluminum substrates. Sample B was modified after anodization by copper electrodeposition.

The first column of Fig. 2 depicts the SEM top-view images of the PEO coatings prepared in the conditions listed in Table 1. They are characterized by an irregular porous structure with pores of different sizes and shapes and no significant differences among the samples. This morphology is a result of the events occurring during the oxide growth under the high electric field: the localized high temperature of discharges that melts the alumina and vaporizes the electrolyte, the inward movement of the electrolyte species, the outward movement of species from the substrate/oxide layer to the solution in the discharge channels, the field-assisted oxide dissolution, and gaseous bubbles evolution. The models used to explain the relationship between the electrical discharges and the porous morphology can be found elsewhere [14,19,35]. The anodization under high voltage usually leads to the formation of two oxide layers: an inner layer, less porous, and an outer layer, more porous due to the intensification of the breakdown events. The SEM side-view images feature the inner and outer layers, although the interfaces between the layers are indistinguishable.

The sample modified by copper electrodeposition after anodization (sample B) exhibited visible black dots over the PEO surface, as seen in the bottom-inset of Fig. 1. These sub-mm-sized dots correspond to approximately 0.2 % of the anodized area of the coating. Fig. 3 shows the micrograph of sample B's dots at different magnifications. Unlike the major portion of sample B's surface exhibiting the porous morphology, these clusters presented a granular structure composed of copper compounds.

The elemental composition of the PEO coatings was evaluated by EDX analysis. Table 2 depicts the percentage of Al, O, Si, and Cu (at.%) on the surface of the oxide layers. The full data and the top-view elemental mapping of samples A, B, and C can be checked in Table C.1 and Fig. C.1 (SI file). The major components of the coating are Al and O, 53–60 at.% and 35–39 at.%, respectively, forming the aluminum oxide layer. The Si content in the coating surfaces varied from 2.5 to 3.4 at.%. The Al/O ratio was maintained approximately constant (1.7) in samples A and B prepared in the same anodizing electrolyte (Table C.2). Sample C exhibited a small reduction in Al/O ratio compared with the other two samples, indicating the anodization in silicate containing copper salt and EDTA led to a major presence of oxygen species related to Al content.

Disregarding the black dot regions of electrodeposits in sample B, the Cu content distributed on the major part of the PEO oxide surface is low, representing 0.1 at.% of the total (Table 2). Sample C also presented a low content of 0.2 at.% in the coating. On the other hand, the mapping performed in an area inside the region of the electrodeposits revealed that the major content is copper (80 at.%), followed by O (10 at.%) and Al (2 at.%), as depicted in Table C.3. However, since the area of copper electrodeposits correspond to only 0.2 % of the PEO surface, the general content of copper over sample B surface still can be considered low. According to Belov et al. [36], the reduction of copper ions over an anodized Al surface occurs locally, accompanied by a high cathodic polarization, as observed in our sample. The formation of a copper layer with high coverage demands a high cathodic current density or a longer electroplating time. Since Cu-content films are more susceptible to corrosion [18], a full coverage was avoided in this study by using moderate electrodeposition conditions, including dilute $Cu(NO_3)_2$ electrolyte and applied potential of −2 V for 10 min.

The other elements presented in the oxide coatings (Na, N, C, and Mg) were incorporated from the electrolyte, except Mg, which

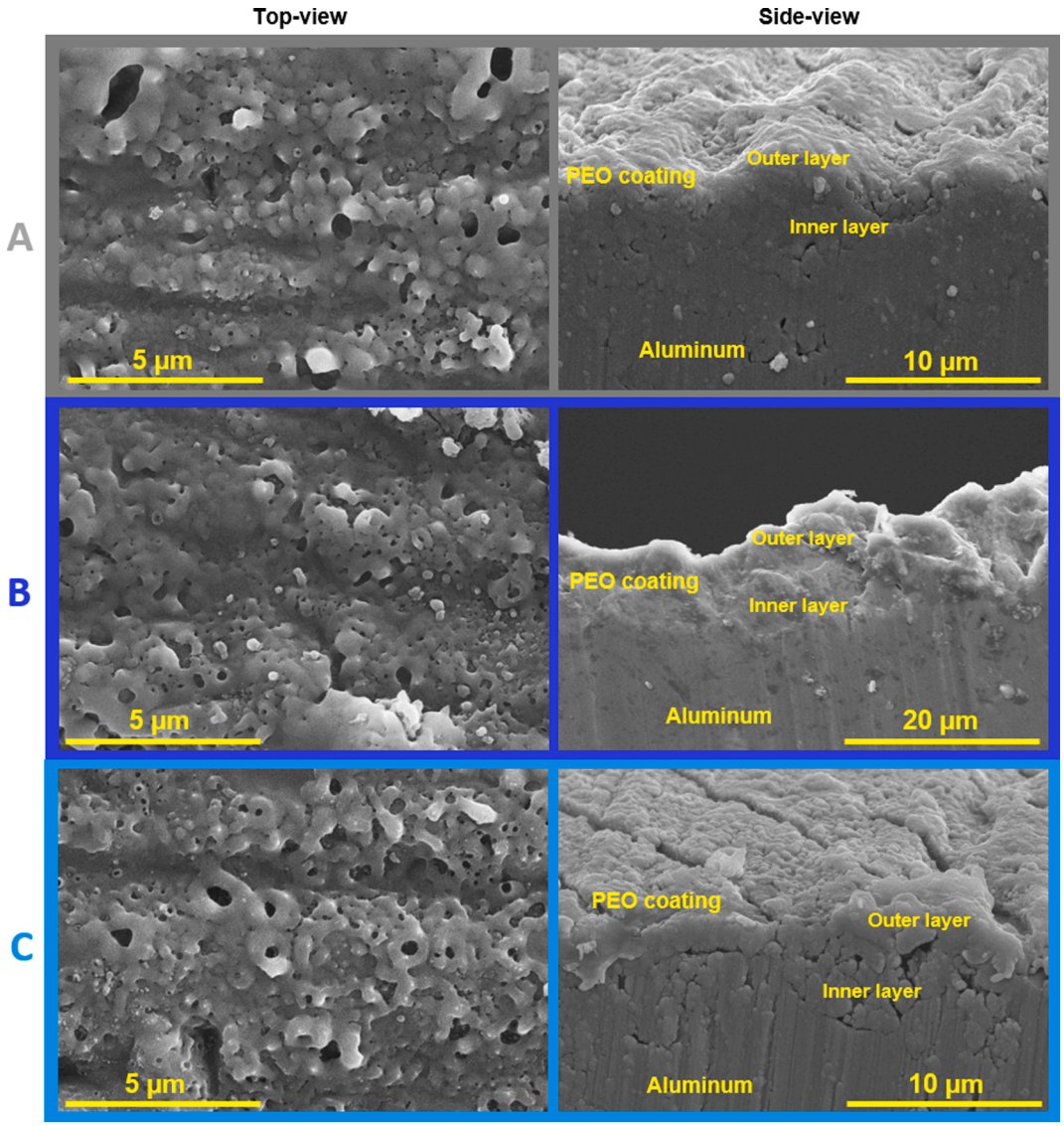

Fig. 2. SEM top-view and side-view images of samples A, B, and C prepared according to experimental conditions listed in Table 1.

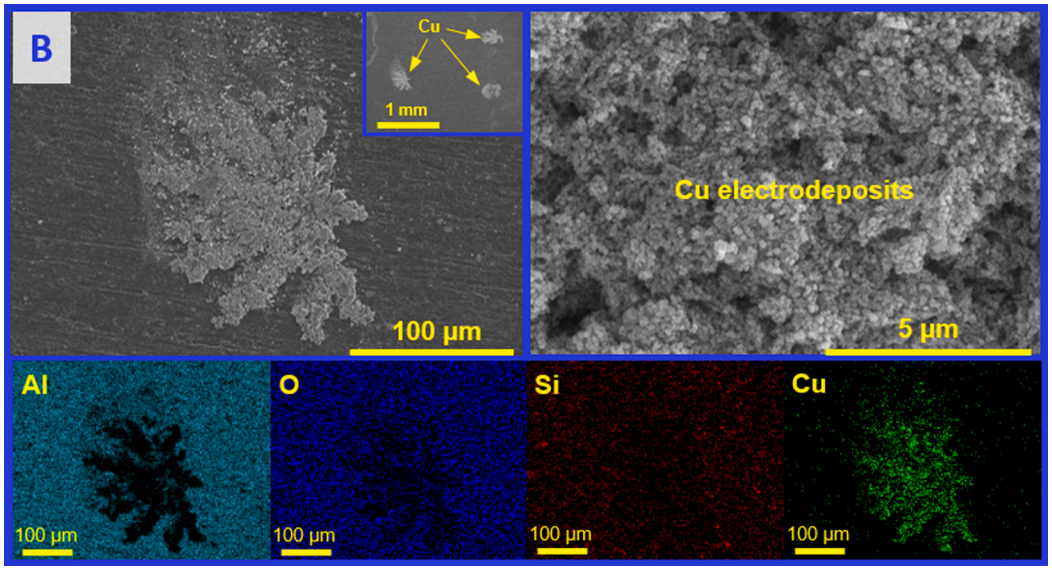

Fig. 3. SEM micrographs (top row) and elemental mapping (bottom row) of a copper cluster over the PEO coating in sample B.

Table 2
EDX semi-quantitative analysis of the PEO coatings prepared by Al anodization in alkaline silicate media.

Sample – Coating		Al / at. %	O / at. %	Si / at. %	Cu / at.%	others / at.%
A	Alumina	59.8 ± 1.1	35.7 ± 0.7	2.5 ± 0.5	—	2.0 ± 0.0
B	Cu-decorated alumina*	60.0 ± 0.1	35.7 ± 0.5	1.6 ± 0.5	0.1 ± 0.0	2.6 ± 0.1
C	Cu-doped alumina	53.1 ± 2.1	39.1 ± 1.0	3.4 ± 0.9	0.2 ± 0.0	4.2 ± 0.1

*Region analyzed outside the copper clusters.

originated from the aluminum alloy (Table A.1). The 1.4–1.8 at.% of Mg in the surface coating illustrates the dynamic of the oxide growth toward and inward the metal/oxide/electrolyte interfaces during the breakdown events.

The elemental mapping of the elements on the surface (Fig. C.1) revealed a homogenous spatial distribution of Al and O outside the pores. On the other hand, Si is concentrated in some surface areas, especially surrounding the pores, resulting from the ejection of molten material during the discharge event since the melting/solidification and diffusion through the channels redistribute the elements in the oxide layer [37]. Unlike sample B, copper presents a homogenous distribution over the surface of sample C.

The X-ray diffractograms of the three samples are depicted in Fig. 4. Despite using a low grazing incident angle ($\theta = 0.4°$) to avoid the beam penetrating too deep into the substrate, the high-intensity peaks observed at $(38.4 \pm 0.1)^o$ and $(44.6 \pm 0.1)^o$ correspond to the (1 1 1) and (2 0 0) peaks of the crystalline substrate, the cubic aluminum, according to the PDF card number 01–089-2837. The other peaks of cubic Al, (2 2 0), (3 1 1), and (2 2 2), were also observed in the three diffractograms at $(64.9 \pm 0.2)^o$, $(78.0 \pm 0.2)^o$, and $(82.2 \pm 0.2)^o$, respectively. The PEO coatings formed on Al alloys in alkaline silicate media usually consist of the metastable γ-Al_2O_3 phase. Herein, the two main peaks of the γ-Al_2O_3 phase were identified at 45.9° (4 0 0) and 67.0° (4 4 0) in the three samples, according to the PDF 00-001-1303. In sample B, decorated with copper by electrodeposition, the main peak of the cubic Cu pattern, (1 1 1), was identified at 43.3°, according to the PDF 98-000-0172, with a low intensity compared to the Al peaks.

Depending on the concentration, the addition of Cu^{2+} ions into the electrolyte during the preparation of sample C could lead to the formation of the thermodynamic stable α-Al_2O_3 phase [38] or other alumina metastable phases (η, χ, δ, κ, and θ) [39]. However, the higher-temperature alumina phases were not identified in the diffractogram of sample C. The low-intensity peak observed at 35.5° might indicate the presence of CuO in this sample; however, its intensity is close to the amplitude of the signal noise, as seen in the figure's inset.

The main peaks of typical crystalline phases of SiO_2 observed in the 2θ range of 20°–30° [40] were not identified. No correspondence with

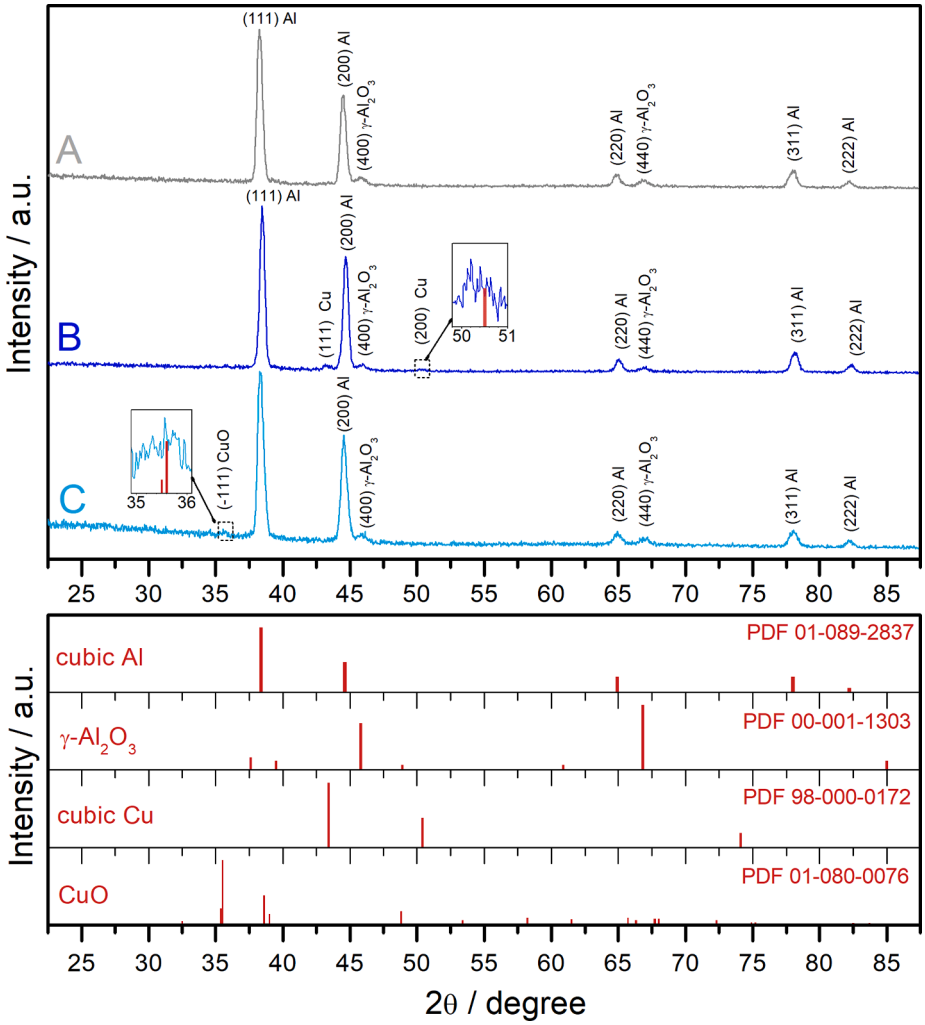

Fig. 4. (*top*) X-ray diffractograms of the PEO samples A, B, and C, prepared according to Table 1. (*bottom*) Standard patterns of cubic aluminum, γ-alumina, cubic Cu, and CuO, as a reference, according to ICDD PDF-2 2021 database.

crystalline aluminosilicate phases like mullite was observed either. Therefore, additional techniques are required to determine the form of silicon content in the coating and identify the copper species. A slight baseline deviation observed in the 20°-30° range, especially in sample C, suggests the presence of amorphous phases.

Fig. 5 depicts XPS spectra of Al 2p, O 1 s, Si 2p, and Cu 2p and the wide survey spectra. The Al 2p spectra of the analyzed samples were deconvoluted into the components (Fig. 5**a**). The two main peaks observed at 74.4 ± 0.3 eV and 75.4 ± 0.3 eV can be attributed to Al^{3+} in the Al_2O_3 and aluminosilicates [37,41], respectively. An additional peak at 78.6 ± 0.0 eV appeared as a shoulder at high binding energy values of the main signal in samples B and C. This peak was also observed in the XPS spectrum of Al in anodized AlCuLi alloys [4,19], but it was not credited to a specific Al bonding since the usual interval of the identification of Al species range from 71 to 77 eV. Instead, this peak can be associated with the overlapping of Cu 3p – Al 2p core levels, as observed in mixed metal oxides [42]. Therefore, this peak at 78.6 eV in samples B and C can be attributed to Cu^{2+} from Cu 3p region spectra. The O 1 s spectra from all three samples were deconvoluted in two peaks (Fig. 5**b**), where the lowest-energy-one (at 531.8 ± 0.1 eV) corresponds to the surface oxygen (O_s) bonding with metallic ions in metal oxides, metal hydroxides, and aluminosilicates [4,41,43]. The oxygen from O-Si bonding in SiO_2 compounds was observed at high binding values (533.1 ± 0.1 eV) [4,44]. The deconvolution of Si 2p spectra from samples A, B, and C showed two peaks (Fig. 5**c**). The peak observed at 102.6 ± 0.0 eV can be attributed to tertiary Al-O-Si compounds forming aluminosilicates [41,43,45], whereas the peak observed at 103.8 ± 0.1 eV can be credited to the Si-O from SiO_2 [4,45]. Considering the XPS spectra of Si 2p and O 1 s and the absence of peaks from Si compounds in the XRD diffractograms, it is probable that the silicon on the film is forming an amorphous phase containing aluminosilicate and silica.

The XPS spectra of Cu 2p related to samples B and C (Fig. 5**d**) depict a doublet peak at binding energy values of 933.1 ± 0.0 eV (Cu $2p_{3/2}$) and 953.2 ± 0.1 eV (Cu $2p_{1/2}$), usually assigned to Cu^{2+} species like CuO and $Cu(OH)_2$ [46,47]. Satellite peaks with low intensity located close to these main peaks can also be observed from the fitting procedure and might indicate multiple oxidation states [46]; however, their intensities have a similar amplitude to the noisy background, which compromises their identification. The overlapping of the metallic copper with the Cu $2p_{3/2}$ peak also makes it difficult to evaluate the individual contribution of the Cu^0 and Cu^{2+} species in the PEO coating. It is possible to assert that both oxidation states (Cu^0 and Cu^{2+}) were presented in sample B. X-rays diffractograms indicated the presence of cubic copper (Cu^0) in the film but not CuO or $Cu(OH)_2$. However, the Cu^{2+} ions probably originated from $Cu(OH)_2$ species. The presence of $Cu(OH)_2$ mixed with metallic Cu in sample B is expected since the copper electrodeposition was performed in acidic $Cu(NO_3)_2$ solution in the absence of buffer with hydrogen evolution reaction (HER) as a side reaction. Under these conditions, the interfacial pH can change, forming hydroxylated species as co-products of the metallic copper reduction [48]. It is possible that part of $Cu(OH)_2$ content could be converted to CuO after drying in the air, but not its majority, since the PEO coatings were not calcinated.

The most probable oxidation states for copper in sample C are the stable Cu^{2+} and Cu^+ at minor extension. According to Şişman et al. [49], the peak with the lowest binding energy value, usually reported in the 932.0–932.7 eV region, can be related to Cu^+ ions in Cu_2O. Therefore, the low-intensity peak observed at 931 eV in sample C, observed from deconvolution of the main peak centered at 933 eV, may indicate a small quantity of Cu^+ forming Cu_2O in the coating.

The wide survey spectra (Fig. 5**e**) of the samples also exhibited a significant C 1 s peak, even in those samples prepared in the absence of EDTA (i.e., samples A and B); however, this peak is regularly ascribed to

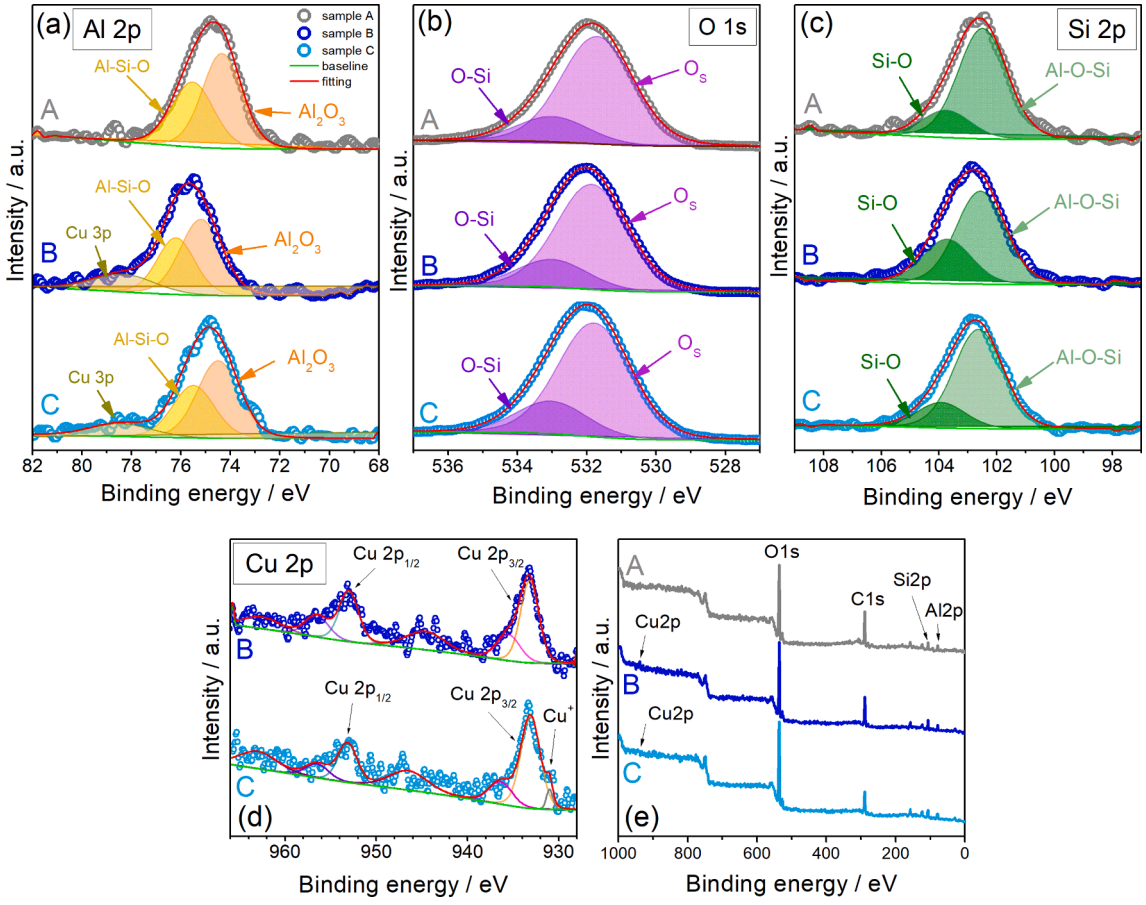

Fig. 5. XPS spectra of (a) Al 2p, (b) O 1 s, (c) Si 2p, and (d) Cu 2p, and the wide survey spectra (e) from samples A, B, and C.

a surface absorption from the air or contamination [41].

FTIR and Raman spectroscopies were carried out to evaluate the bonding structure of the various coating materials, and the results are shown in Fig. 6. The FTIR spectra of the substrate and three oxide samples presented similar characteristics except in the 820–620 cm^{-1} range (Fig. 6**a**), where both Al-O and Cu-O bonds can be detected. The peaks in the 1000–500 cm^{-1} range indicate the absorption from Al-O groups [50,51], while vibrations of the Cu-O bond can be identified in the 830−620 cm^{-1} range [52]. The spectra of samples B and C suggest the overlapping of the bands, forming intense broadband, which was not observed in sample A and the bare AA5052 substrate. It is important to stress that the aluminum alloy forms a passive thin layer of aluminum oxide with a few nanometers thickness when exposed to air [10]; therefore, Al-O bonds are also expected in the bare substrate.

The absorption peaks related to asymmetric stretching of the Si-O-Si bonds are located in the 1200 – 1000 cm^{-1} range [53]. In samples A and C, this peak is observed at 1025 cm^{-1}, while in sample B, it is more intense and observed at 1036 cm^{-1}. The symmetric stretching of the Si-O-Si bond [54] is identified at 830 cm^{-1} in sample A, but it is not seen in samples B and C due to the overlapping of the peaks related to Al-O and Cu-O bonds forming the above-mentioned broadband. Bending vibrations of O-Cu-O bonds can also be observed at 830−820 cm^{-1} [52] and could contribute to the band's widening in the 820–620 cm^{-1} range, being more intense in the samples containing copper (B and C).

The wide band observed in all samples at 3600 – 3000 cm^{-1} is assigned to the stretching vibration of the O-H bond. Additionally, the peaks observed at approximately 2167, 2027, and 1966 cm^{-1} can be related to the additional vibrational bands of hydroxyl groups present in the mineral forms of aluminum hydroxides [55–57]. These peaks indicated that the oxide is partially hydrated in the anodized sample as well as in the native oxide covering the bare substrate. The peaks at 2968, 2357, 1732, and 1224 cm^{-1} can be assigned to HCO_3^- bond vibrations from CO_2 and H_2O adsorbed from the air [58,59].

Since they follow different selection rules, Raman bands are considered complementary to the IR bands and can confirm the presence of amorphous phases. Fig. 6b depicts the Raman spectra of samples A, B, and C split into two regions, namely the 200–1400 cm^{-1} and 2900–3400 cm^{-1} ranges. At first glance, the general view of the Raman spectra of the PEO coatings in the first region resembles the Raman spectra of aluminosilicate glasses, as reported elsewhere [60,61]. Compared with the broader bands usually observed in the spectra of those glasses with centers around 490, 600, 800, and 1100 cm^{-1}, herein, these bands are wider and present a superposition of several peaks, which indicate the presence of different phases in the PEO coatings besides the amorphous aluminosilicate.

The Raman bands in the 400–700 cm^{-1} region can be attributed to the bending vibrations of TO_4 groups and T-O-T linkages (T = Al or Si), with an additional band at ~ 800 cm^{-1} due to the rearrangement of the Si-O-Al network [61]. The 700–800 cm^{-1} region is characterized by intra- and inter-tetrahedral deformation modes and AlO_4 stretching vibrations [61]. Raman modes around 1100 cm^{-1} can be assigned to asymmetric and symmetric stretching vibrations of polymerized tetrahedral network $Si(OAl)_y$ units where *y* corresponds to the number of AlO_4 tetrahedra connected to a SiO_4 tetrahedron and to (Si,Al)-NBO and (Si,Al)-BO stretch bands (where NBO = non-bridging O atoms; BO = bridging O atoms) [60]. The presence of amorphous silica can be identified in the PEO coatings by the Raman vibrational modes near 1170 cm^{-1} and 1220 cm^{-1}. The former band overlapped with those attributed to the silicate band, but the second band, observed at 1216–1234 cm^{-1} in the three spectra, can evidence the presence of amorphous silica.

Regarding the aluminum oxide, no Raman peaks for γ-Al_2O_3 and δ-Al_2O_3 phases are usually observed in the low-frequency region [62], which makes this technique useful for evaluating amorphous alumina or aluminum (oxy)hydroxide species. FTIR spectra showed evidence of aluminum hydroxide species, which can be confirmed by the broader peaks in the high-frequency region. The bands centered at ~ 3007 and ~ 3200 cm^{-1} can be assigned to the hydroxyl stretching (μ-OH) [63]. The presence of copper could be identified in sample B at 287 cm^{-1}, and it can be assigned to Cu^{2+} species [46].

In summary, the material analysis demonstrated that the porous PEO coatings consisted mainly of the crystalline γ-Al_2O_3 phase identified by XRD. Despite no detection of a crystalline aluminosilicate phase, XPS, FTIR, and Raman scattering data indicated the presence of amorphous phases of aluminosilicate, silica, and aluminum hydroxides. The silicon content is distributed over all surfaces, although deposits were found concentrated around the pores. A model for silica deposition from silicate in alkaline media was proposed by Wang et al. [37]. SEM-EDX analysis of sample B demonstrated that the copper content in the Cu-decorated film (sample B) consisted of electrodeposits of metallic copper and $Cu(OH)_2$ formed during the electrodeposition process as a side reaction of copper reduction. The Cu^0 species were identified by XRD, whereas Cu^{2+} species were detected by XPS and Raman spectroscopy. The major content of copper formed clusters (sub-mm dots) randomly distributed on the PEO coating and comprising a total area of 0.2 % of the surface. In the Cu-doped film (sample C), the copper content consisted of Cu^{2+} species incorporated into the film, as was identified by

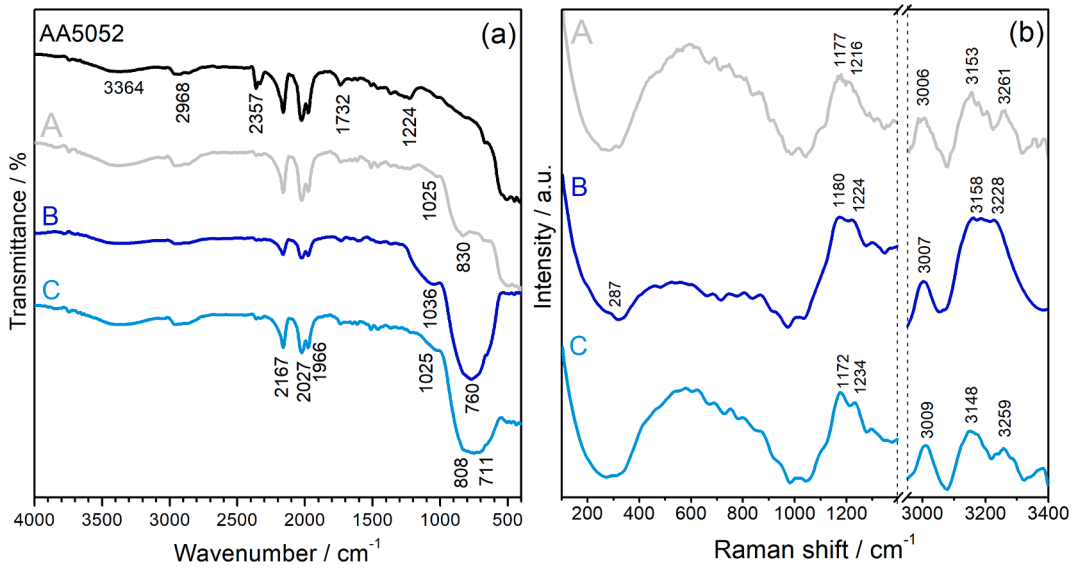

Fig. 6. (a) FTIR spectra of the AA5052 substrate and the PEO coatings (samples A, B, and C). (b) Raman scattering spectra of the PEO coatings.

XRD and XPS, while a small amount of Cu^{+} ions was detected in XPS Cu 2p spectra. The total content of copper in this sample was 0.2 at.%, and it was homogeneously distributed on the coating surface, as seen in the SEM mapping.

Additionally to the material characterization, the wetting behavior of the coatings was evaluated by water contact angle measurements since the hydrophilic/hydrophobic behavior can influence the bacterial adhesion to the metal oxide surfaces [64]. Fig. 7 shows the CA results of the three samples and substrate. Considering the error bars, the three samples and substrate present similar mild hydrophilic behavior. The CA values range from 80.3° (sample A) to 89.3° (sample B) on average, close to the transition from hydrophilic to hydrophobic behavior (see Table D.1 for details).

These values are higher than those reported by other studies involving PEO coatings produced over aluminum alloys in alkaline silicate media. Arunnellaiappan et al. [65], for instance, observed a superhydrophilicity value of 24° and attributed it to the presence of the micropores. Yang et al. [66] observed CA values of 9° and 40° credited to the large number of pores and cracks on the outer oxide layer compared with sealed samples. Herein, the CA values showed that the AA5052 substrate and PEO coating surfaces had a similar water affinity, with no significant variation. As discussed previously, a similarity regarding surface chemical bonds could be observed among the samples and substrate (Fig. 6**a**). On the other hand, the native oxide film formed in contact of the aluminum alloy with the air is compact, rigid, and thin, which differs from the porous, rough, and thicker PEO coatings. Therefore, the CA results imply that the nature of the chemical bonds influenced wettability at the surface rather than the morphology.

3.2. Corrosion performance evaluation

The corrosion behavior of the PEO coatings was analyzed in polarized and steady-state conditions by PDP and EIS measurements in 3 wt% NaCl solution (pH 6.2), a moderate aggressive medium. Fig. 8 depicts the polarization curves obtained at 1 mV s^{-1} and Table 3 presents the corrosion potential (E_{corr}) and the corresponding values of corrosion current density (j_{corr}) extracted from the polarization curves by the Tafel extrapolation method.

Generally, E_{corr} reflects the corrosion tendency of the material, while j_{corr} can indicate the presence of a corrosion barrier, like a passive layer, for instance. High corrosion potential and low corrosion current usually demonstrate high corrosion resistance [45]. However, additional features like the porous nature of the PEO coatings and other surface properties should be taken into account to evaluate their overall corrosion performance. From the analysis of corrosion potential, it is observed that the copper-free PEO coating (sample A) presented the best corrosion resistance with a positive corrosion potential of + 0.38 V *vs* SHE, while the alloy substrate exhibited E_{corr} = −0.35 V *vs* SHE (Table 3). Both copper-alumina samples demonstrated intermediate corrosion resistance. The E_{corr} values of sample B (Cu-decorated film) and sample C (Cu-doped film) were −0.10 V and −0.12 V *vs* SHE,

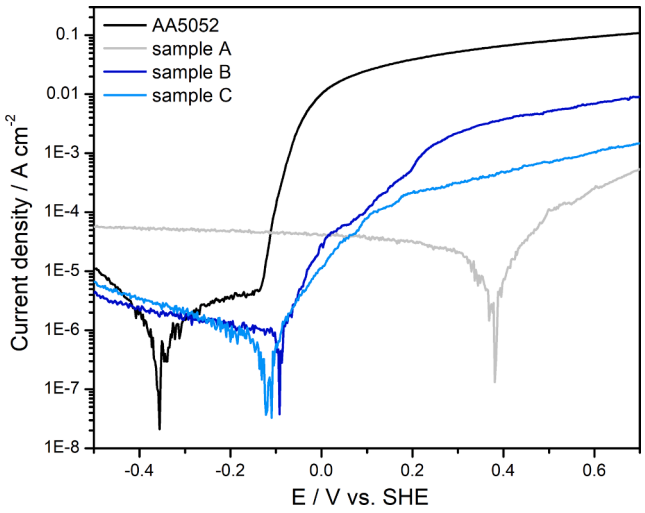

Fig. 8. Potentiodynamic polarization curves of aluminum alloy substrate and the PEO coatings obtained in 3 wt% NaCl solution at 1 mV s^{-1}.

Table 3
Corrosion potential (E_{corr}) and current densities (j_{corr}) of the bare substrate and PEO coatings extracted from PDP curves and electrical components of the equivalent circuits to fit the EIS data measured from OCP in 3 wt% NaCl after 24 h of immersion into the solution.

Sample	Coating	E_{corr} *vs* SHE / V	j_{corr} / μA cm^{-2}	R_1 / kΩ cm^2	R_2 / kΩ cm^2
AA5052	Bare substrate	−0.35	0.6	37.4	30.8*
A	Alumina	+0.38	14.3	11.7	200.1
B	Cu-decorated alumina	−0.10	0.8	17.9	38.0
C	Cu-doped alumina	−0.12	0.7	4.6	31.7

*In the bare substrate, R_2 is associated with the inductance component.

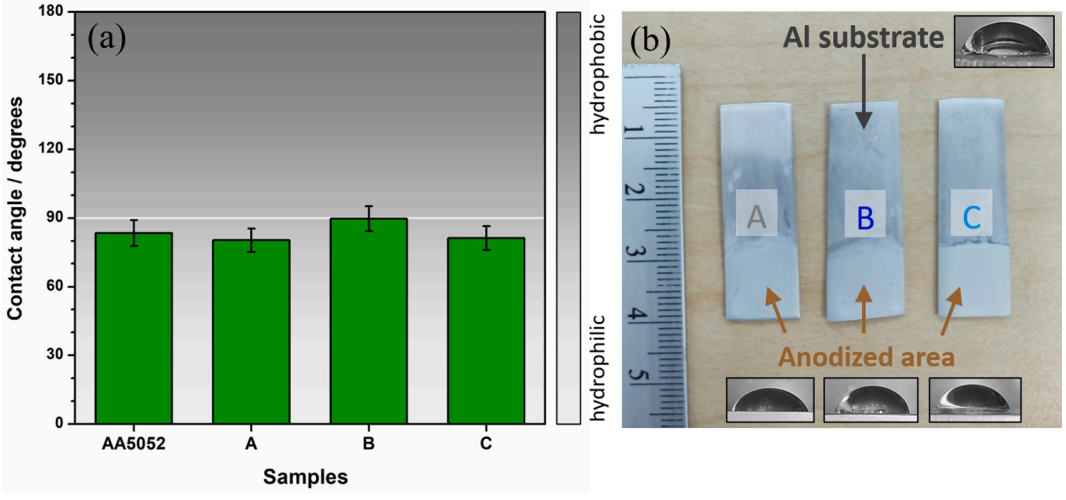

Fig. 7. (a) Water contact angles measured on the untreated AA5052 substrate and PEO coating surfaces of the samples A, B, and C prepared according to Table 1. (b) Optical images of the aluminum specimens exhibiting the anodized area and the corresponding water drop images registered during the CA measurements.

respectively. The addition of copper diminished the corrosion resistance of the PEO coatings. The reduction of corrosion potential promoted by copper insertion into the PEO coating was also reported by Cerchier et al. [3] and attributed to the nobleness difference between copper and aluminum and their effect on galvanic corrosion. The j_{corr} values, in the microampere range, indicate the localized corrosion of the AA5052 substrate and PEO coatings in samples A, B, and C. The alumina film, sample A, exhibited a corrosion current density higher (14.3 μA cm^{-2}) than the bare substrate and both copper-alumina coatings (0.6–0.8 μA cm^{-2}).

Table E.1 (SI file) shows the concentration of the metal leached into the solution after the PDP tests analyzed by the ICP-OES technique. The results show that the concentration of Al and Mg from AA5052 alloy in the solution is high without the protective PEO coating (606.9 ± 20.9 and 14.0 ± 0.2 mg/L, respectively). The Al and Mg concentrations in the solution decreased significantly after PDP tests carried out with samples A, B, and C. But it is not possible to identify which layer these elements originated from since both alloy substrate and coating contained these metals. However, the small amounts of Si and Cu indicated the corrosion of the PEO coatings at some extent.

The corrosion performance of the PEO coatings was also evaluated at steady-state condition using EIS after 24 h of immersion in 3 wt% NaCl solution. Fig. 9 depicts the Bode and Nyquist plots obtained at OCP. Bode plots (Fig. 9**a**) showed that the impedance (Z) is higher at lower frequencies. Impedance data at high frequencies is associated with the corrosion characteristics of the outer layer of the PEO coating, whereas the corrosion behavior of the inner layer is described by impedance values of the low-frequency region [67,68]. Since the inner layer is the principal responsible for the corrosion resistance, it can be asserted from the low-frequency region of the Bode plots that sample A exhibited the higher capacitive behavior and, consequently, the better corrosion resistance (Z ~ 10^5 Ω cm^{-2}), as observed in the PDP tests. The alloy substrate, covered with only the native oxide layer, presented the smallest impedance values over the entire frequency range, indicating the lowest corrosion resistance, which is compatible with its metallic conductive character. Comparing the two Cu-content samples, sample B presented the highest Z value at lower frequency compared with sample C, but this condition reversed at higher frequencies. At high frequencies (10^4–10^5 Hz), the impedance values of sample C were close to the Cu-free alumina coating (sample A).

To estimate the resistance values of the oxide layers in the coatings, the EIS data were analyzed by fitting them to electrical equivalent circuits (EC) based on some physical models for Al PEO coatings proposed in the literature [18,65,69]. Fig. 9**b-c** exhibit the Nyquist plots with the fitting curves. Fig. 9**d** depicts the EC used to represent the AA5052 substrate. The EC used to simulate the capacitance behavior of samples A and C is illustrated in Fig. 9**e**, whereas the EC employed to represent sample B is shown in Fig. 9**f**. The Nyquist plot of the AA5052 substrate consisted of a single capacitive loop at high frequencies and an inductive loop at low frequencies. The capacitive loop is attributed to the charge transfer process and pitting corrosion of the Al alloy, whereas the inductive loop is credited to the adsorption/desorption of species from the aluminum corrosion [69,70]. Its equivalent circuit comprises three resistances (R_s, R_1, R_2), one constant phase element (CPE_1), and the inductive element, L (Fig. 9**d**). R_s is the solution resistance, common to all equivalent circuits. In the bare substrate, R_1 is the resistance associated with the CPE_1, representing a non-ideal capacitance behavior of the alloy covered with the native passive film. R_2 is the resistance in parallel with the inductance and represents the inductive resistance of adsorbed species in the localized defective sites [71] of the native oxide film. The values of each element extracted from the fitting of the AA5052 spectrum are listed in Table E.1 (SI file).

A common model applied to the Al PEO coatings considers that the coating consists mainly of two layers: a porous outer layer and a less porous inner layer (or a compact barrier layer). The inner layer is considered responsible for the material's corrosion protection. The corresponding EC for this model is exhibited in Fig. 9**e** and consists of three resistances (R_s, R_1, R_2) and two constant phase elements (CPE_1 and CPE_2). The CPE is usually applied to represent a defective, inhomogeneous, and rough interface [69]. In this case, CPE_1 and its resistance R_1 represent the outer layer of the PEO coating, whereas CPE_2 and R_2 can be associated with the inner layer. This equivalent circuit was used to fit the EIS spectra of samples A and C (alumina coating and Cu-doped alumina coating, respectively). For sample B (Cu-decorated coating), CPE_3 and R_3 elements were added in the equivalent circuit (Fig. 9**f**) to account to account for the adsorption and electron transfer processes

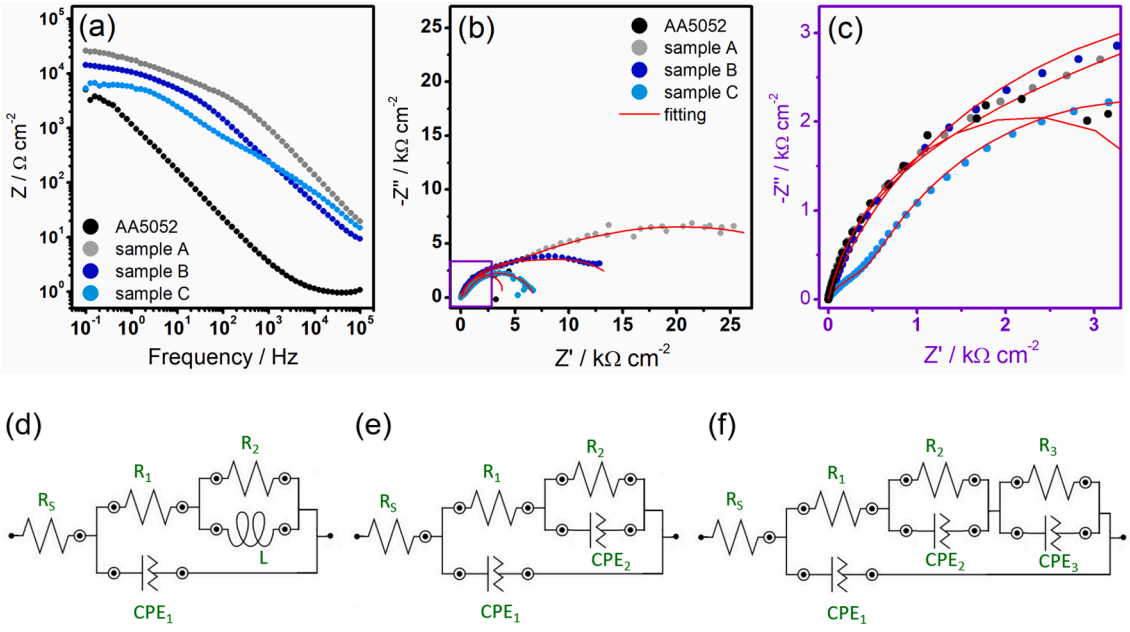

Fig. 9. Electrochemical impedance spectra of the AA5052 substrate and samples A, B and C obtained in 3 wt% NaCl solution at OCP after immersion for 24 h into the solution: (a) Bode plots, (b) wide Nyquist plots, and (c) Nyquist plots in the high-frequency region. The equivalent circuits used to fit the EIS spectra of (d) AA5052 substrate, (e) samples A and C, and (f) sample B.

occurring in the additional phase formed by the copper electrodeposits. The Nyquist plots show that these EC models fitted the data well at high frequencies with a slight deviation at low frequencies due to the dispersion points observed in this region. Nonetheless, the EC models constitute a good approach for estimating the resistance associated with the oxide layers and observing the system trends.

Table 3 shows the values of R_1 and R_2 of samples A, B, and C, associated with the resistance of the outer and inner layers of the PEO coatings, respectively. Table E.2 (SI file) shows the complete data with the values of each element extracted from the EIS fitting. Note that sample A exhibits the highest value of resistance of the inner layer (R_2), responsible for the anticorrosion performance of the coating, and the highest capacitive behavior. This result corroborated the PDP tests.

3.3. Antimicrobial tests

The antimicrobial activity of the PEO coatings was evaluated using *E. coli* and *S. aureus* bacteria as a model for gram-negative and gram-positive bacteria, respectively. These two types of bacteria differ in their cell wall structure, which affects their inactivation mechanism. The gram-positive bacteria present a thick cell wall, while the gram-negative bacteria present a cell wall 4–5 times thinner and are more susceptible to mechanical lysis and osmotic rupture [72].

Fig. F.1 depicts the results of the antimicrobial tests against *E. coli* performed in triplicates after 24 h of incubation in contact with samples A, B, and C. The number of viable cells can be counted visually in the Petri dishes using the plate counting method [28]. Compared with the concentration of colonies at $t = 0$ h, a significant reduction of *E. coli* colonies after 24 h for the samples containing copper (B and C) was observed. The percentage of reduction calculated according to Eq. (1) is shown in Fig. 10**a** and Table F.1. The results show that the bacteria concentration reduced by 86.3 ± 6.0 % after 24 h in contact with the Cu-free PEO coating (sample A) and diminished by 98.4 ± 2.1 % and 100 % in the tests with samples B and C, that is, the Cu-decorated and Cu-doped PEO coatings, respectively. Fig. F.2 depicts the antimicrobial tests against *S. aureus*, where the drastic reduction of bacteria colonies after 24 h in contact with the three samples can be observed. The results showed a reduction of 99.9 ± 0.0 %, 100 %, and 100 % for samples A, B, and C, respectively (Table F.1). This is an outstanding result not only for the Cu-content coatings but also for the Cu-free alumina film (sample A).

On the other hand, when the antimicrobial activity is considered, sample A did not present an effective activity. Unlike the percentage of reduction, the antimicrobial activity is calculated using an untreated sample as a reference. This means that despite sample A exhibiting a high percentage of reduction for both bacteria types, the coating is considered ineffective compared to the reference. According to the JIS Z 2801:2006 test, the antimicrobial activity values were calculated using Eq. (2), and only samples with values equal to or higher than 2 present antimicrobial effectiveness. Note that samples B and C present higher antimicrobial activity for both bacteria types. The Cu-decorated coating (sample B) exhibited higher antimicrobial activity for the gram-positive *S. aureus* bacteria. In contrast, the Cu-doped coating (sample C) presented a higher antimicrobial activity for the gram-negative *E. coli* bacteria. The tests demonstrated a small variability among the triplicates, especially for *S. aureus*, except for sample B, which presented the largest deviation in the *E. coli* tests (note the relatively large error bar in Fig. 10**b**). Despite this significant deviation, the interval of antimicrobial activity for this sample remained above the dotted line, representing the limit between antimicrobial ineffectiveness and effectiveness.

The antibacterial activity of the Cu-free PEO coating (sample A) can be attributed to Al_2O_3 and SiO_2 phases. Both species are not considered potential antimicrobial agents but present, to some extent, antibacterial properties. Some studies involving nanoparticles and bulk Al_2O_3 have shown a mild antibacterial activity against some microorganisms, although their effectiveness depends on the oxide concentration, surface area, particle size, crystalline structure, and bacteria cell wall [73–75]. For instance, inhibition zone growth tests demonstrated an antibacterial effect for the gram-positive *Bacillus cereus* and *Bacillus subtilis* bacteria but no effect on gram-negative *Vibrio cholerae* and *Klebsiella pneumonia* [74]. Another study revealed a mild growth-inhibitory effect against *E. coli*, but only at very high alumina concentration [75]. Regarding SiO_2, a study demonstrated death rates of 40 % for gram-positive *B. subtilis* and death rates of 58 % and 70 % for *E. coli* and *Pseudomonas fluorescent* (gram-negatives) [76]. Several models are proposed in the literature to explain the inactivation mechanisms of these metal oxides, like the surface charge interactions between positively charged particles at near-neutral pH and the negatively charged bacteria wall cells. The electrostatic interaction led to the adhesion of nanoparticles on the bacteria surface, inducing mechanical damage and the osmotic rupture of their cells [76]. Another mechanism is based on the interaction of the metal ion with the thiol, amino, and carboxylic groups of proteins present in the cell wall of bacteria leading to their denaturation and causing cell death [76]. Regarding PEO coatings, the antimicrobial activity of alumina films was demonstrated only in coatings containing other antimicrobial agents as an additive, like silver or copper, and the antimicrobial effect was usually attributed to the antimicrobial agent

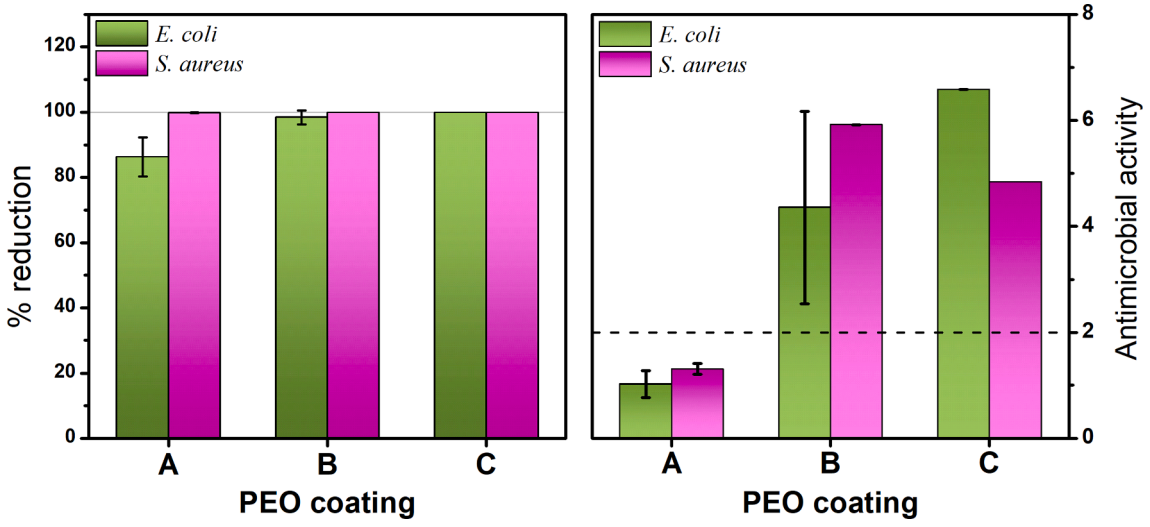

Fig. 10. (a) Percent bacteria reduction and (b) antimicrobial activity of the PEO coatings against *E. coli* and *S. aureus* for sample A (alumina film), sample B (Cu-decorated alumina film), and sample C (Cu-doped alumina film).

[3,9,43].

Herein, the addition of copper into the alumina films led to outstanding improvement of antimicrobial activity. Copper compounds are excellent antimicrobial agents being toxic to a large number of bacteria types. Both bulk and nanoparticle forms of copper oxides present strong antibacterial activity. Studies suggest that their action is based on the release of Cu^{+} and Cu^{2+} ions and their interactions with specific groups in the proteins of bacteria cell walls [77]. These interactions can be via the production of reactive oxygen species or by electrostatic attraction leading to protein denaturation and cell death.

In this study, the bacterial inactivation mechanisms for the Cu-content PEO coatings take into account the different architectures and oxidation states of copper species. Sample B exhibits clusters at specific regions of the surface composed of metallic copper and copper hydroxides. These regions can release Cu^{2+} ions if a bacterium enters into contact with the particle surface and is adsorbed by the bacterium cell wall, exposing the metallic copper particles. When the surface of metallic Cu is exposed to air, the metal is readily oxidized, forming more $Cu_xO/Cu(OH)_2$ species, which can be released if another bacterium enters into contact. The continuous release of copper ions can be responsible for the antimicrobial effect by contact killing [78].

On the other hand, in the porous region outside the copper clusters, as well as in the Cu-doped film, the presence of copper ions, silica and alumina can provide an antimicrobial activity via copper ions release and electrostatic interactions of Al_2O_3 and SiO_2 particles with the bacterium cell wall. In this sense, the Cu-decorated sample has two types of centers to attack the bacteria, namely the clusters and the bulk porous region. This could be a reason for its excellent bacterial effect against gram-positive bacteria, which present a thicker and more resistant cell wall.

Some remarks about the copper added to the alumina PEO coatings should be taken into account regarding its effect on antimicrobial activity and corrosion performance. The results showed that copper addition significantly improved the coatings' antimicrobial activity but, as a consequence, decreased their corrosion resistance. It is well-established in the literature that the inner layer mainly promotes corrosion resistance of PEO coatings against the aggressive ions. In contrast, the outer layer is more susceptible to corrosion attack when the coating is not sealed. In this sense, the possible strategies to increase the corrosion resistance of the coating are to seal the pores, fill them with anticorrosive materials, or enlarge the inner layer. The former strategy is recommended when anticorrosive protection is essential but diminishes the active surface area of the coating and requires additional fabrication steps. Herein, the sealing could be a disadvantage since the porous structure can act as a reservoir of antimicrobial agents [29]. The larger the surface area, the larger the number of sites available for contact killing and bacteria inactivation.

Another factor that can be considered is the presence of OH^{-} ions in the electrolyte during the anodization. As discussed previously, the role of the OH^{-} in the electrolyte is to increase the oxygen content and decrease the solution resistance. But the results showed that the oxygen content was higher in the absence of OH^{-} and the anodization faster. Therefore, the following question is addressed: Are OH^{-} ions necessary for the process? The results indicate that OH^{-} may be important for enlargement of the inner layer, despite reducing the anodization rate and making the experiment longer. The longer the system was maintained at a lower voltage, the more time was available for the growth of the inner layer. Under the conditions used, it was not possible to identify the limits between the layers and estimate their thickness. Still, from R_1 and R_2 values from the EIS fitting, we could determine resistance values, a parameter directly associated with the layer thickness. Therefore, a two-step anodization could be an alternative to fabricating Cu-doped alumina films with a thicker inner layer in a hydroxide-free electrolyte. The first step, limited to low voltages (<30 V) for a specific time, could assure the inner layer enlargement, followed by a second step, i.e., the anodization at higher voltages to achieve the PEO condition. Other strategies to increase the quality of the PEO coatings include anodizing using AC or pulsed modes using the mild conditions, as proposed in this study.

Restraining the system to mild conditions is important cause PEO is considered an environmentally friendly technique that uses an electrochemical process and non-toxic chemicals to produce a metal finishing. However, the high-power consumption is still a drawback for large-scale production, especially for larger anodized specimens. In this study, we proposed a synthetic route for anodizing in PEO conditions at voltages (350–370 V) lower than those commonly employed in the PEO of aluminum (400–700 V [9,21,72]) and using low concentration of reagents to offer a cost-effective alternative to antimicrobial PEO coating production.

The strategies adopted in this study showed great potential for fabricating antimicrobial surfaces over aluminum with small copper content with remarkable antimicrobial activity for both bacteria tested. Additionally, copper compounds have also demonstrated an excellent ability to inactivate other microorganisms like fungi [3] and viruses [78,79], implying that PEO coatings containing copper are promising materials for different surfaces. Further studies are still necessary to enhance the corrosion performance of the functional coatings; we discussed some strategies above. However, it is important to stress that the corrosion performance was evaluated by electrochemical methods in an aggressive aqueous medium. The proposed application of these synthesized materials does not involve their use in an aqueous environment but antimicrobial aluminum surfaces of materials in contact with the air, such as doors, handrails, and knobs in public areas, as well as medical utensils and household materials. Therefore, both Cu-content coatings can offer good protection and excellent antimicrobial activity for these applications.

4. Conclusions

In this study, we proposed facile, environmentally friendly, and cost-effective synthetic routes for fabricating PEO coatings over aluminum alloy (AA5052), aiming at self-disinfecting surface applications, where copper was chosen as the antimicrobial agent. The copper was inserted into the alumina films via electrodeposition and anodic doping methodologies. The following conclusions can be drawn from this study:

- Under the experimental conditions used, the oxide coatings grew over the AA5052 surface producing two porous layers (an outer and a less porous inner layer). The coating consisted of a crystalline γ-Al_2O_3 phase and amorphous phases of aluminosilicates, SiO_2, and $Al(OH)_3$. Cu-content coatings presented a lower copper content (<0.3 at.%). Cu-decorated film exhibited visible black dots on the porous surface, where Cu^{0} and Cu^{2+} species were identified. The Cu-doped film presented Cu^{2+} and Cu^{+} distributed on the oxide surface.
- The composition and architecture of the PEO coatings exerted a direct influence on the corrosion performance and bacterial inactivation mechanism.
- The corrosion resistance of 5052 aluminum alloy significantly improved with the PEO treatment. However, the copper addition decreased the corrosion performance of the resulting materials in aggressive aqueous medium. Comparing both Cu-content films, the Cu-decorated PEO coating presented higher corrosion resistance. On the other hand, the Cu-doped alumina film exhibited good stability against metastable pitting formation in corrosive solution.
- Both Cu-decorated and Cu-doped synthesized films exhibited outstanding bactericide effectiveness with a low content of the antimicrobial agents. Cu-decorated film showed a major effect against the gram-positive *S. aureus* bacteria (antimicrobial activity = 5.92), whereas the Cu-doped film exhibited high antimicrobial activity (6.58) for the gram-negative *E. coli* bacteria. The results indicated that the bacterial inactivation mechanisms differed in both

samples and can be associated with the chemical composition of the coatings.

CRediT authorship contribution statement

Janaina S. Santos: Conceptualization, Methodology, Investigation, Formal analysis, Writing – original draft. **Victor Márquez:** Methodology, Investigation, Formal analysis. **Josephus G. Buijnsters:** Writing – review & editing, Supervision. **Supareak Praserthdam:** Writing – review & editing, Supervision, Resources. **Piyasan Praserthdam:** Supervision, Project administration, Resources, Funding acquisition.

Declaration of Competing Interest

The authors declare that they have no known competing financial interests or personal relationships that could have appeared to influence the work reported in this paper.

Data availability

Data will be made available on request.

Acknowledgments

This research project is supported by the Second Century Fund (C2F), Chulalongkorn University, Thailand, and the National Research Council of Thailand (NRCT).

Appendix A. Supplementary data

Supplementary data to this article can be found online at https://doi.org/10.1016/j.apsusc.2022.155072.

References

[1] H. Kawakami, K. Yoshida, Y. Nishida, Y. Kikuchi, Y. Sato, Antibacterial properties of metallic elements for alloying evaluated with application of JIS Z 2801:2000, ISIJ Int. 48 (2008) 1299–1304, https://doi.org/10.2355/isijinternational.48.1299.
[2] C. Vargel, Corrosion of Aluminium, second ed., Elsevier, Amsterdam, 2020.
[3] P. Cerchier, L. Pezzato, C. Gennari, E. Moschin, I. Moro, M. Dabalà, PEO coating containing copper: A promising anticorrosive and antifouling coating for seawater application of AA7075, Surf. Coat. Technol. 393 (2020), 125774, https://doi.org/10.1016/j.surfcoat.2020.125774.
[4] Z. Zhu, W. Tu, Y. Cheng, Y. Cheng, The formation of metallic W and amorphous phase in the plasma electrolytic oxidation coatings on an Al alloy from tungstate-containing electrolyte, Surf. Coat. Technol. 361 (2019) 176–187, https://doi.org/10.1016/j.surfcoat.2019.01.024.
[5] D. Zhang, Q. Han, K. Yu, X. Lu, Y. Liu, Z. Lu, Q. Wang, Antibacterial activities against Porphyromonas gingivalis and biological characteristics of copper-bearing PEO coatings on magnesium, J. Mater. Sci. Technol. 61 (2021) 33–45, https://doi.org/10.1016/j.jmst.2020.05.025.
[6] C.H. Ferreira, S.C. Nunes, V.A.Q. Santos, E.C. Pereira, M.S. Sikora, Plasma electrolytic titanium oxide applied for pathogenic bacteria inactivation, Environ. Technol. 41 (2020) 141–152, https://doi.org/10.1080/09593330.2018.1491641.
[7] T.W. Clyne, S.C. Troughton, A review of recent work on discharge characteristics during plasma electrolytic oxidation of various metals, Int. Mater. Rev. 64 (2019) 127–162, https://doi.org/10.1080/09506608.2018.1466492.
[8] X. Liu, S. Wang, N. Du, X. Li, Q. Zhao, Evolution of the three-dimensional structure and growth model of plasma electrolytic oxidation coatings on 1060 aluminum alloy, Coatings. 8 (2018) 105, https://doi.org/10.3390/coatings8030105.
[9] J.S. Santos, A. Rodrigues, A.P. Simon, C.H. Ferreira, V.A.Q. Santos, M.S. Sikora, N. C. Cruz, G.P. Mambrini, F. Trivinho-Strixino, One-step synthesis of antibacterial coatings by plasma electrolytic oxidation of aluminum, Adv. Eng. Mater. 21 (2019) 1900119, https://doi.org/10.1002/adem.201900119.
[10] F. Trivinho-Strixino, J.S. Santos, M. Souza Sikora, 3 - Electrochemical synthesis of nanostructured materials, in: A.L. Da Róz, M. Ferreira, F. de Lima Leite, O.N. Oliveira (Eds.), Nanostructures, William Andrew Publishing, 2017, pp. 53-103. https://doi.org/10.1016/B978-0-323-49782-4.00003-6.
[11] J.S. Santos, S.G. Lemos, W.N. Gonçalves, O.M. Bruno, E.C. Pereira, Characterization of electrical discharges during spark anodization of zirconium in different electrolytes, Electrochim. Acta 130 (2014) 477–487, https://doi.org/10.1016/j.electacta.2014.03.052.
[12] S. Wang, Y. Gu, Y. Geng, J. Liang, J. Zhao, J. Kang, Investigating local corrosion behavior and mechanism of MAO coated 7075 aluminum alloy, J. Alloys and Compd. 826 (2020), 153976, https://doi.org/10.1016/j.jallcom.2020.153976.
[13] W. Yang, B. Jiang, A. Wang, H. Shi, Effect of negatively charged ions on the formation of microarc oxidation coating on 2024 aluminium alloy, J. Mater. Sci. Technol. 28 (2012) 707-712. https://doi.org/10.1016/S1005-0302(12)60119-4.
[14] R.O. Hussein, X. Nie, D.O. Northwood, A. Yerokhin, A. Matthews, Spectroscopic study of electrolytic plasma and discharging behaviour during the plasma electrolytic oxidation (PEO) process, J. Phys. D Appl. Phys. 43 (2010), 105203, https://doi.org/10.1088/0022-3727/43/10/105203.
[15] P. Cerchier, L. Pezzato, E. Moschin, L.B. Coelho, M.G.M. Olivier, I. Moro, M. Magrini, Antifouling properties of different plasma electrolytic oxidation coatings on 7075 aluminium alloy, Int. Biodeter. Biodegr. 133 (2018) 70–78, https://doi.org/10.1016/j.ibiod.2018.06.005.
[16] L. Agureev, S. Savushkina, A. Ashmarin, A. Borisov, A. Apelfeld, K. Anikin, N. Tkachenko, M. Gerasimov, A. Shcherbakov, V. Ignatenko, N. Bogdashkina, Study of plasma electrolytic oxidation coatings on aluminum composites, Metals. 8 (2018) 459, https://doi.org/10.3390/met8060459.
[17] W. Dai, C. Li, C. Zhang, L. Chen, Z. Li, H. Zhang, Y. Zhang, Effect of Cu on microarc oxidation coated Al–xCu alloys, Surf. Eng. 37 (2021) 1098–1109, https://doi.org/10.1080/02670844.2021.1942413.
[18] L. Zhu, W. Zhang, T. Zhang, J. Qiu, J. Cao, F. Wang, Effect of the Cu content on the microstructure and corrosion behavior of PEO coatings on Al–xCu alloys, J. Electrochem. Soc. 165 (2018) C469–C483, https://doi.org/10.1149/2.0471809jes.
[19] Y.-L. Cheng, Z.-G. Xue, Q. Wang, X.-Q. Wu, E. Matykina, P. Skeldon, G. E. Thompson, New findings on properties of plasma electrolytic oxidation coatings from study of an Al–Cu–Li alloy, Electrochim. Acta 107 (2013) 358–378, https://doi.org/10.1016/j.electacta.2013.06.022.
[20] T. Wu, C. Blawert, M.L. Zheludkevich, Influence of secondary phases of $AlSi_9Cu_3$ alloy on the plasma electrolytic oxidation coating formation process, J. Mater. Sci. Technol. 50 (2020) 75–85, https://doi.org/10.1016/j.jmst.2019.12.031.
[21] D. Kim, D. Sung, J. Lee, Y. Kim, W. Chung, Composite plasma electrolytic oxidation to improve the thermal radiation performance and corrosion resistance on an Al substrate, Appl. Surf. Sci. 357 (2015) 1396–1402, https://doi.org/10.1016/j.apsusc.2015.10.003.
[22] S.-K. Wu, W. Yang, W. Gao, Y.-H. Yao, Y. Zhang, J. Chen, Characterization of MAO + Cu composite coatings on aluminum alloy, Coatings. 11 (2021) 1172, https://doi.org/10.3390/coatings11101172.
[23] J.S. Santos, F. Trivinho-Strixino, E.C. Pereira, The influence of experimental conditions on the morphology and phase composition of Nb-doped ZrO_2 films prepared by spark anodization, Corros. Sci. 73 (2013) 99–105, https://doi.org/10.1016/j.corsci.2013.03.029.
[24] D.A. Becerik, A. Ayday, L.C. Kumruoğlu, S.C. Kurnaz, A. Özel, The effects of Na_2SiO_3 concentration on the properties of plasma electrolytic oxidation coatings on 6060 aluminum alloy, J. Mater. Eng. Perform. 21 (2012) 1426–1430, https://doi.org/10.1007/s11665-011-0022-1.
[25] W.J. Stępniowski, K.-K. Wang, S. Chandrasekar, D. Paliwoda, A. Nowak-Stępniowska, W.Z. Misiolek, The impact of ethylenediaminetetraacetic acid (EDTA) additive on anodization of copper in $KHCO_3$ – hindering Cu^{2+} re-deposition by EDTA influences morphology and composition of the nanostructures, J. Electroanal. Chem. 87 (2020), 114245, https://doi.org/10.1016/j.jelechem.2020.114245.
[26] W.S. Rasband, ImageJ version 1.53s, U. S. National Institutes of Health, Bestheda, Maryland, USA, 1997-2018. https://imagej.nih.gov/ij/.
[27] J.I. Standard, JIS Z 2801 Antimicrobial products - Test for antimicrobial activity and efficacy, in: Japanese Standards Association, Japan, 2000.
[28] M.L. Bari, S. Yeasmin, Microbes Culture Methods, in: N. Rezaei (Ed.), Encyclopedia of Infection and Immunity, Elsevier, 2021. https://doi.org/10.1016/B978-0-12-818731-9.00128-2.
[29] A. Nastruzzi, F. Cicerchia, A. Fortini, C. Nastruzzi, Gold hard anodized (GHA) materials with antimicrobial surface properties: mechanical, tribological, and microbiological characterization, Emerg. Mater. 4 (2021) 249–263, https://doi.org/10.1007/s42247-021-00180-y.
[30] D.S. Tsai, C.C. Chou, Review of the soft sparking issues in plasma electrolytic oxidation, Metals. 8 (2018) 105, https://doi.org/10.3390/met8020105.
[31] A.L. Yerokhin, A.A. Voevodin, V.V. Lyubimov, J. Zabinski, M. Donley, Plasma electrolytic fabrication of oxide ceramic surface layers for tribotechnical purposes on aluminium alloys, Surf. Coat. Technol. 110 (1998) 140–146, https://doi.org/10.1016/S0257-8972(98)00694-X.
[32] A.L. Yerokhin, X. Nie, A. Leyland, A. Matthews, S.J. Dowey, Plasma electrolysis for surface engineering, Surf. Coat. Technol. 122 (1999) 73–93, https://doi.org/10.1016/S0257-8972(99)00441-7.
[33] V.P. Parkhutik, J.M. Albella, J.M. Martinez-Duart, Electric breakdown in anodic oxide films, in: B.E. Conway, J.O.M. Bockris, R.E. White (Eds.), Moderns Aspects of Electrochemistry, Plenum Press, New York, 1992, pp. 315–391.
[34] J.M. Albella, I. Montero, J.M. Martinez-Duart, Theory of avalanche breakdown during anodic oxidation, Electrochim. Acta 32 (1987) 255–258, https://doi.org/10.1016/0013-4686(87)85032-6.
[35] D.-D. Wang, X.-T. Liu, Y.-K. Wu, H.-P. Han, Z. Yang, Y. Su, X.-Z. Zhang, G.-R. Wu, D.-J. Shen, Evolution process of the plasma electrolytic oxidation (PEO) coating formed on aluminum in an alkaline sodium hexametaphosphate ($(NaPO_3)_6$) electrolyte, J. Alloys Compd. 798 (2019) 129–143, https://doi.org/10.1016/j.jallcom.2019.05.253.
[36] D.V. Belov, M.V. Maximov, S.N. Belyaev, T.I. Devyatkina, G.A. Gevorgyan, Effect of azo compounds on the structure and mechanical properties of a copper coating electrodeposited on oxidized aluminum alloys, Inorg. Mater. Appl. Res. 12 (2021) 1386–1399, https://doi.org/10.1134/S2075113321050051.

[37] S. Wang, X. Liu, X. Yin, N. Du, Influence of electrolyte components on the microstructure and growth mechanism of plasma electrolytic oxidation coatings on 1060 aluminum alloy, Surf. Coat. Technol. 381 (2020), 125214, https://doi.org/10.1016/j.surfcoat.2019.125214.

[38] V.V. Subbotina, U.F. Al-Qawabeha, O.V. Sobol, V.V. Belozerov, V.V. Schneider, T. A. Tabaza, S.M. Al-Qawabah, Increase of the alpha-Al_2O_3 phase content in MAO-coating by optimizing the composition of oxidated aluminum alloy, Funct. Mater. 26 (2019) 752–758. https://doi.org/10.15407/fm26.04.752.

[39] N.M. Stuart, K. Sohlberg, The microstructure of γ-alumina, Energies. 14 (2021) 6472, https://doi.org/10.3390/en14206472.

[40] I.G. Polyakova, 4. The main silica phases and some of their properties, in: J.W.P. Schmelzer (Ed.) Glass: Selected Properties and Crystallization, De Gruyter, 2014, pp. 197-268.

[41] L. Pezzato, M. Dabalà, S. Gross, K. Brunelli, Effect of microstructure and porosity of $AlSi_{10}Mg$ alloy produced by selective laser melting on the corrosion properties of plasma electrolytic oxidation coatings, Surf. Coat. Technol. 404 (2020), 126477, https://doi.org/10.1016/j.surfcoat.2020.126477.

[42] F. Li, L. Zhang, D.G. Evans, X. Duan, Structure and surface chemistry of manganese-doped copper-based mixed metal oxides derived from layered double hydroxides, Colloids Surf. A Physicochem. Eng. Asp. 244 (2004) 169–177, https://doi.org/10.1016/j.colsurfa.2004.06.022.

[43] P. Cerchier, L. Pezzato, K. Brunelli, P. Dolcet, A. Bartolozzi, R. Bertani, M. Dabalà, Antibacterial effect of PEO coating with silver on AA7075, Mater. Sci. Eng. C 75 (2017) 554–564, https://doi.org/10.1016/j.msec.2017.02.084.

[44] J.-L. Wang, W. Yang, D.-P. Xu, X.-F. Yao, Effect of $K_2TiO(C_2O_4)_2$ addition in electrolyte on the microstructure and tribological behavior of micro-arc oxidation coatings on aluminum alloy, Acta Metall. Sin-Engl. 30 (2017) 1109–1118, https://doi.org/10.1007/s40195-017-0641-0.

[45] C. Du, S. Huang, X. Yu, Q. Wang, H. Zhao, Microstructure and properties of plasma electrolytic oxidation coating on 55% SiC_p/Al matrix composites, Surf. Coat. Technol. 420 (2021), 127321, https://doi.org/10.1016/j.surfcoat.2021.127321.

[46] W.J. Stępniowski, D. Paliwoda, S.T. Abrahami, M. Michalska-Domańska, K. Landskron, J.G. Buijnsters, J.M.C. Mol, H. Terryn, W.Z. Misiolek, Nanorods grown by copper anodizing in sodium carbonate, J. Electroanal. Chem. 857 (2020), 113628, https://doi.org/10.1016/j.jelechem.2019.113628.

[47] D.P.O. Jerez, M.L. Teijelo, W.R. Cervantes, O.E.L. Pérez, J. Sánchez, G.C. Pizarro, G. Acosta, M. Flores, R. Arratia-Perez, Nanostructuring of anodic copper oxides in fluoride-containing ethylene glycol media, J. Electroanal. Chem. 807 (2017) 181–186, https://doi.org/10.1016/j.jelechem.2017.11.047.

[48] E.B. Carneiro-Neto, M.C. Lopes, E.C. Pereira, Simulation of interfacial pH changes during hydrogen evolution reaction, J. Electroanal. Chem. 765 (2016) 92–99, https://doi.org/10.1016/j.jelechem.2015.09.029.

[49] O. Şişman, N. Kılınç, Z.Z. Öztürk, Structural, electrical and H_2 sensing properties of copper oxide nanowires on glass substrate by anodization, Sens. Actuators B Chem. 236 (2016) 1118–1125, https://doi.org/10.1016/j.snb.2016.06.148.

[50] L. Feng, H. Zhang, P. Mao, Y. Wang, Y. Ge, Superhydrophobic alumina surface based on stearic acid modification, Appl. Surf. Sci. 257 (2011) 3959–3963, https://doi.org/10.1016/j.apsusc.2010.11.143.

[51] I. Vrublevsky, K. Chernyakova, A. Bund, A. Ispas, U. Schmidt, Effect of anodizing voltage on the sorption of water molecules on porous alumina, Appl. Surf. Sci. 258 (2012) 5394–5398, https://doi.org/10.1016/j.apsusc.2012.02.020.

[52] A.M. Abd-Elnaiem, M.A. Abdel-Rahim, A.Y. Abdel-Latief, A.A. Mohamed, K. Mojsilović, W.J. Stępniowski, Fabrication, characterization and photocatalytic activity of copper oxide nanowires formed by anodization of copper foams, Materials. 14 (2021) 5030, https://doi.org/10.3390/ma14175030.

[53] L. Pezzato, P. Cerchier, K. Brunelli, A. Bartolozzi, R. Bertani, M. Dabalà, Plasma electrolytic oxidation coatings with fungicidal properties, Surf. Eng. 35 (2019) 325–333, https://doi.org/10.1080/02670844.2018.1441659.

[54] L. Pezzato, M. Rigon, A. Martucci, K. Brunelli, M. Dabalà, Plasma Electrolytic Oxidation (PEO) as pre-treatment for sol-gel coating on aluminum and magnesium alloys, Surf. Coat. Technol. 366 (2019) 114–123, https://doi.org/10.1016/j.surfcoat.2019.03.023.

[55] F.K. Silva, R.A.A.B. Santa, M.A. Fiori, T.F.d. Aquino, C. Soares, M.A.P.M. Martins, N. Padoin, H.G. Riella, Synthesis of aluminum hydroxide nanoparticles from the residue of aluminum anodization for application in polymer materials as antiflame agents, J. Mater. Sci. Technol. 9 (2020) 8937-8952. https://doi.org/10.1016/j.jmrt.2020.05.108.

[56] J.D. Russell, V.C. Farmer, D.G. Lewis, Lattice vibrations of boehmite (γ-AlOOH): Evidence for a C_{2v}^{12} rather than a D_{2h}^{17} space group, Spectrochim. Acta A Mol, Spectrosc. 34 (1978) 1151–1153, https://doi.org/10.1016/0584-8539(78)80073-7.

[57] İ. Boz, Ö. Kerkez, Effects of boehmite synthesis conditions on the epoxidation of styrene, React. Kinet. Mech. Catal. 100 (2010) 237–247, https://doi.org/10.1007/s11144-010-0177-z.

[58] D. Zeng, Z. Liu, S. Bai, J. Wang, Influence of sealing treatment on the corrosion resistance of PEO Coated Al-Zn-Mg-Cu alloy in various environments, Coatings. 9 (2019) 867, https://doi.org/10.3390/coatings9120867.

[59] L. Telmenbayar, A.G. Ramu, D. Yang, M. Song, T.-O. Erdenebat, D. Choi, Corrosion resistance of the anodization/glycidoxypropyltrimethoxysilane composite coating on 6061 aluminum alloy, Surf. Coat. Technol. 403 (2020), 126433, https://doi.org/10.1016/j.surfcoat.2020.126433.

[60] D.R. Neuville, L. Cormier, V. Montouillout, P. Florian, F. Millot, J.C. Rifflet, D. Massiot, Structure of Mg- and Mg/Ca aluminosilicate glasses: ^{27}Al NMR and Raman spectroscopy investigations, Am. Mineral. 93 (2008) 1721–1731, https://doi.org/10.2138/am.2008.2867.

[61] I. Daniel, P. Gillet, B.T. Poe, P.F. McMillan, In-situ high-temperature Raman spectroscopic studies of aluminosilicate liquids, Phys. Chem. Miner. 22 (1995) 74–86, https://doi.org/10.1007/BF00202467.

[62] A. Roy, A.K. Sood, Phonons and fractons in sol-gel alumina: Raman study, Pramana 44 (1995) 201–209, https://doi.org/10.1007/BF02848471.

[63] X. Zhang, P.L. Huestis, C.I. Pearce, J.Z. Hu, K. Page, L.M. Anovitz, A. B. Aleksandrov, M.P. Prange, S. Kerisit, M.E. Bowden, W. Cui, Z. Wang, N. R. Jaegers, T.R. Graham, M. Dembowski, H.-W. Wang, J. Liu, A.T. N'Diaye, M. Bleuel, D.F.R. Mildner, T.M. Orlando, G.A. Kimmel, J.A. La Verne, S.B. Clark, K. M. Rosso, Boehmite and gibbsite nanoplates for the synthesis of advanced alumina products, ACS Appl. Nano Mater. 1 (2018) 7115–7128, https://doi.org/10.1021/acsanm.8b01969.

[64] B. Li, B.E. Logan, Bacterial adhesion to glass and metal-oxide surfaces, Colloids Surf. B Biointerfaces 36 (2004) 81–90, https://doi.org/10.1016/j.colsurfb.2004.05.006.

[65] T. Arunnellaiappan, S. Arun, S. Hariprasad, S. Gowtham, B. Ravisankar, L. R. Krishna, N. Rameshbabu, Fabrication of corrosion resistant hydrophobic ceramic nanocomposite coatings on PEO treated AA7075, Ceram. Int. 44 (2018) 874–884, https://doi.org/10.1016/j.ceramint.2017.10.014.

[66] D. Yang, D. Gerelt Od, A.G. Ramu, D. Choi, Fabrication of enhanced corrosion protection of PEO/PFOTES nanocomposite film coatings on aluminum alloy deposited by plasma electrolytic oxidation, Mater. Lett. 315 (2022), 131898, https://doi.org/10.1016/j.matlet.2022.131898.

[67] Z. Yang, R.-Q. Wang, C. Liu, Y.-K. Wu, D.-D. Wang, X.-T. Liu, X.-Z. Zhang, G.-R. Wu, D.-J. Shen, The electrochemical corrosion behavior of plasma electrolytic oxidation coatings fabricated on aluminum in silicate electrolyte, J. Mater. Eng. Perform. 28 (2019) 3652–3660, https://doi.org/10.1007/s11665-019-04099-8.

[68] A. Sobolev, T. Peretz, K. Borodianskiy, Synthesis and growth mechanism of ceramic coatings on an Al-Cu alloy using plasma electrolytic oxidation in molten salt, J. Alloys Compd. 869 (2021), 159309, https://doi.org/10.1016/j.jallcom.2021.159309.

[69] R. Aliramezani, K. Raeissi, M. Santamaria, A. Hakimizad, Characterization and properties of PEO coatings on 7075 Al alloy grown in alkaline silicate electrolyte containing $KMnO_4$ additive, Surf. Coat. Technol. 329 (2017) 250–261, https://doi.org/10.1016/j.surfcoat.2017.09.056.

[70] Q. Huang, L. Liu, Z. Wu, S. Ji, H. Wu, P. Chen, Z. Ma, Z. Wu, R.K.Y. Fu, H. Lin, X. Tian, F. Pan, P.K. Chu, Corrosion-resistant plasma electrolytic oxidation coating modified by Zinc phosphate and self-healing mechanism in the salt-spray environment, Surf. Coat. Technol. 384 (2020), 125321, https://doi.org/10.1016/j.surfcoat.2019.125321.

[71] N. Xiang, R.G. Song, H. Li, C. Wang, Q.Z. Mao, Y. Xiong, Study on microstructure and electrochemical corrosion behavior of PEO coatings formed on aluminum alloy, J. Mater. Eng. Perform. 24 (2015) 5022–5031, https://doi.org/10.1007/s11665-015-1766-9.

[72] M.A. Subhan, Chapter 13 - Antibacterial property of metal oxide-based nanomaterials, in: S. Rajendran, A. Mukherjee, T.A. Nguyen, C. Godugu, R.K. Shukla (Eds.), Nanotoxicity, Elsevier, 2020, pp. 283-300. https://doi.org/10.1016/B978-0-12-819943-5.00013-0.

[73] M. Bhuvaneshwari, S. Bairoliya, A. Parashar, N. Chandrasekaran, A. Mukherjee, Differential toxicity of Al_2O_3 particles on gram-positive and gram-negative sediment bacterial isolates from freshwater, Environ. Sci. Pollut. Res. 23 (2016) 12095–12106, https://doi.org/10.1007/s11356-016-6407-9.

[74] G. Geoprincy, N.N. Gandhi, S. Renganathan, Novel antibacterial effects of alumina nanoparticles on *bacillus cereus* and *bacillus subtilis* in comparison with antibiotics, Int. J. Pharm. Pharm. Sci. 4 (2012) 544–548.

[75] I.M. Sadiq, B. Chowdhury, N. Chandrasekaran, A. Mukherjee, Antimicrobial sensitivity of *Escherichia coli* to alumina nanoparticles, Nanomed. Nanotechnol. Biol. Med. 5 (2009) 282–286, https://doi.org/10.1016/j.nano.2009.01.002.

[76] W. Jiang, H. Mashayekhi, B. Xing, Bacterial toxicity comparison between nano- and micro-scaled oxide particles, Environ. Pollut. 157 (2009) 1619–1625, https://doi.org/10.1016/j.envpol.2008.12.025.

[77] V. Stanić, S.B. Tanasković, Chapter 11 - Antibacterial activity of metal oxide nanoparticles, in: S. Rajendran, A. Mukherjee, T.A. Nguyen, C. Godugu, R. K. Shukla (Eds.), Nanotoxicity, Elsevier, 2020, pp. 241–274.

[78] V. Govind, S. Bharadwaj, M.R. Sai Ganesh, J. Vishnu, K.V. Shankar, B. Shankar, R. Rajesh, Antiviral properties of copper and its alloys to inactivate covid-19 virus: a review, Biometals 34 (2021) 1217–1235, https://doi.org/10.1007/s10534-021-00339-4.

[79] S.L. Warnes, C.W. Keevil, Inactivation of norovirus on dry copper alloy surfaces, PLoS ONE 8 (2013) e75017.